

## Microwave spectroscopy of high- $L$ , $n = 10$ Rydberg states of helium

E. A. Hessels,\* P. W. Arcuni,† F. J. Deck, and S. R. Lundeen

*Department of Physics, University of Notre Dame, Notre Dame, Indiana 46556*

(Received 31 December 1991)

Intervals between the  $10G$ ,  $H$ ,  $I$ ,  $K$ , and  $L$  ( $L=4-8$ ) states of helium have been measured with high precision using a fast-beam microwave-laser technique. The uncertainties in the measured intervals are less than 1 kHz (or about  $10^{-13}$  a.u.) for each of the 16 intervals. The measurements are compared with precise theoretical predictions and are used to test relativistic, QED, and retardation effects in these states. The measurements confirm the contributions from “retardation forces” to better than 10%.

PACS number(s): 32.30.Bv, 31.30.Jv

### I. INTRODUCTION

Precision spectroscopy of high- $L$  Rydberg states of helium provides tests of fundamental aspects of two-electron atoms and of physically large atoms. The measurements described here between  $(1s)(nl)$  states of helium (with  $n=10$  and  $L$  ranging from 3 to 8) are among the most accurate measurements for any states in the helium atom, and are the most precise measurements on any large ( $r \gtrsim 100a_0$ ) atom. An experimental precision of a few tenths of a kilohertz ( $10^{-13}$  Ry) has been achieved for the energy intervals between these states. The experimental values can be compared to theoretical predictions of these states from two independent calculations [1,2] which use two very different methods in determining the energies.

The present measurement is the latest in a series of measurements of increasing accuracy on these high- $L$   $n=10$  states [3–6]. A brief report of the experimental results has been given earlier [7].

An energy-level diagram for these states is shown in Fig. 1. The diagram shows the separations between states of different  $L$ , which is predominantly due to the interaction between the polarizable  $\text{He}^+$  core and the distant Rydberg electron. The lowest-order potential due to this interaction is

$$V_{\text{dipole pol}} = -\frac{1}{2}e^2\alpha_1/r^4, \quad (1)$$

where  $\alpha_1$  is the dipole polarizability of  $\text{He}^+$  and  $r$  is the radial coordinate of the Rydberg electron. The figure also shows the separation between states of the same  $L$ , which is due to spin-orbit and spin-spin interactions. This structure consists of four nearly equally spaced levels, unlike the singlet-triplet groupings at lower  $L$  where the exchange energies are large.

The measurements are of interest for a variety of reasons, most of which are related to the size of the atoms. The first, and the one which inspired this program of measurements, is the possibility of seeing effects due to retardation (or so-called Casimir forces). Retardation effects have been of interest to physicists since Casimir and Polder showed in 1948 [8] that the usual  $r^{-6}$  Van der Waals potential between two neutral atoms

changes to an  $r^{-7}$  potential for large  $r$  when the effects of retardation are included. All attempts to observe this effect experimentally, or similar effects in wall-wall, electron-wall, electron-electron, and electron-atom interactions, have failed to give precision measurements of the effects [9,10]. The retardation potential for an ion-electron system (such as helium) was first described by Kelsey and Spruch in 1978 [11], who predicted a potential of

$$V_{\text{KS}} = \frac{11}{4\pi} \frac{\hbar}{mc} e^2 \alpha_1 / r^5, \quad (2)$$

which was predicted to be valid for  $n \gtrsim (1/\alpha)^{1/2}$ . This potential is due to the exchange of two photons (at least one of which is transverse) between the Rydberg electron and  $\text{He}^+$  core. The effect is much smaller than the  $r^{-4}$  polarizability potential (and, of course, very much smaller than the  $r^{-1}$  Coulomb potential), but should have been observable in Rydberg states of helium. In response to the suggestion of Spruch, the  $n=10$ ,  $L=4-7$  levels of helium were precisely measured by Palfrey and Lundeen [3] and their energies were calculated in a long-range polarization model by Drachman [12]. Comparison between these two showed that the predicted retardation effect was not present. It was later shown by Au, Feinberg, and Sucher [13] that the asymptotic  $r^{-5}$  was in fact not appropriate for these  $n=10$  states, and that the contribution due to retardation was one order of magnitude smaller than that obtained using the  $r^{-5}$  potential. In response, the precision of the measurements was improved by about one order of magnitude [5]. The present measurement represents almost another order of magnitude improvement, which puts the precision at the level of a few percent of the retardation effect to these  $n=10$  states, and a few tenths of a percent of the natural linewidths of the  $n=10$  fine-structure transitions. The present measurements can also be used to test the precise calculations of Drake for these states [2], and in particular to test the relativistic and QED corrections for these large atoms.

## II. EXPERIMENTAL TECHNIQUE

The technique used for measuring these high- $L$   $n = 10$  states is similar to that used by Palfrey in his earlier measurements of these states [14,3] and in subsequent experiments on these states [4-6]. A schematic of the experiment is shown in Fig. 2. A 13-keV ion beam is created and focused at (1) in Fig. 2 and is directed at a charge-exchange cell at (2) where most of the beam is neutralized by charge exchange with a few mTorr of argon gas. Those atoms not neutralized are deflected out of the beam at (3). The 10-kV/cm field at (3) also serves to ionize and deflect high- $n$  ( $n \geq 20$ ) atoms, which would otherwise contribute to background current in our detector. Some of the atoms are in  $n = 10$  states, and these can be excited up to  $n = 30$  by means of a CO<sub>2</sub> laser transition at

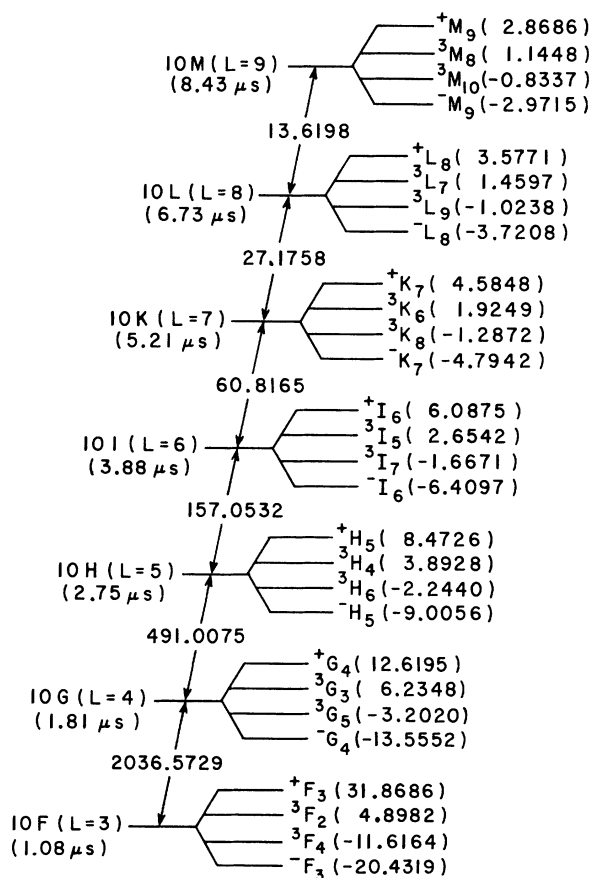


FIG. 1. Energy-level diagram for the high- $L$  states of  $n = 10$  helium. The notation used is  $10^{2S+1}L_J$ , where  $S$  is the total electron spin and  $J$  is the total of the spin  $S$  and the orbital angular momentum  $L$ . The two  $J = L$  states are labeled  $10^\pm L_J$  since for these states  $S$  is not a good quantum number and the eigenstates are (for  $L > 3$ ) approximately odd and even linear combinations of the singlet and triplet states. The lifetimes of the states are given in parentheses. The energy separations between the mean  $10L$  positions (the statistically weighted averages of the energies of four levels and of the energy of each state relative to this mean energy) are given in MHz and represent the best theoretical values, obtained from a variety of calculations [2,1,20,13,28,30].

(4) or (8). The laser is a cw, single-frequency CO<sub>2</sub> laser tuned by varying the angle of intersection between the laser and neutral beams and thus varying the Doppler shift. The resulting  $n = 30$  atoms are then Stark ionized at (9) and the resulting ions are deflected and detected by a channel electron multiplier. The 180-MHz resolution of the laser resonance (which is consistent with the expected resolution for the 3-mrad divergence of the atomic beam) is sufficient to resolve the  $10G$ - $30H$  transitions and to partially resolve the  $10H$ - $30I$  transition, but is not sufficient to resolve the higher- $L$  states, as shown in Fig. 3. In order to make high-precision measurements of transitions between  $n = 10$  states, we use the main rf region shown at (6) in Fig. 2. The first laser is then used to depopulate a particular  $n = 10$  state (for example,  $10H$ ) so that a large population difference exists for the  $10I$ -to- $10H$  rf transition at (6). The  $10H$  atoms which result from this rf transition are excited up to  $n = 30$  by the second laser and are then ionized and detected. Thus an rf transition at (6) produces an increase in the ion current at the detector. The rf is 100% amplitude modulated, and the ion current synchronous with this modulation is the rf signal, as measured with a lock-in amplifier. This signal is measured at a range of frequencies near each of the resonance frequencies, and the data are fit to obtain a center for each of the resonance features.

For the higher- $L$  states, this depopulation and detection scheme fails since the higher- $L$  laser transitions are unresolved (see Fig. 3). To solve this problem, two auxiliary rf regions are added at (5) and (7) of Fig. 2. The purpose of these regions is to transfer the population of a high- $L$  state to a lower- $L$  state which is resolved by the laser. For example, to observe the  $10^-K_7$ -to- $10^-I_6$  transition in the main rf region, the auxiliary regions are set to the  $10^-I_6$ -to- $10^-H_5$  transition. Since these auxiliary regions resolve the individual magnetic-fine-structure (MFS) component, they also select out individual peaks in the main resonance scans and thus reduce the effects due to overlapping resonances [6].

The main rf interaction region is a 3-m-long rf transmission line with the rf propagating in a TEM mode along the same axis as the neutral helium beam. The 3-m length of the region was necessary to obtain the desired interaction time of  $3.75 \mu\text{s}$ . This time gives a time-of-flight linewidth of 250 kHz, which is sufficient to resolve the individual magnetic-fine-structure resonances quite well. The transmission line (shown in Fig. 4) consists of a  $\frac{1}{2}$ -in. diam. cylindrical copper inner conductor and a copper WR229 waveguide as an outer conductor, with the position of the inner conductor chosen to make the characteristic impedance of the line equal to  $50 \Omega$ . Since any impedance mismatch along the length or at the exit of the transmission line would cause reflected waves, and since these waves, which propagate in the opposite direction relative to the beam, cause shifts in the measured line centers, it was desirable to minimize the size of the mismatches. To keep the relative positions of the inner and outer conductors fixed along the distance of the 3-m region (and thus the impedance constant), it was necessary to fasten the inner conductor to the outer with

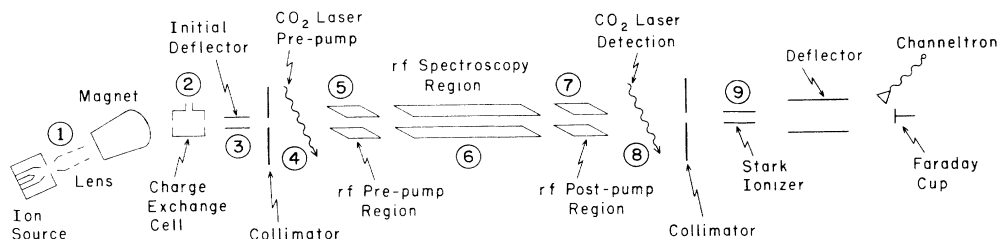


FIG. 2. A schematic of the experiment. Fast atoms are created by charge exchange between a 13-keV ion beam and a neutral gas target at 2. Those atoms not neutralized are deflected out of the beam at 3. Atoms in  $n = 10$  states are excited up to  $n = 30$  using a  $\text{CO}_2$  laser, both at 4 (to deplete the population of a  $10L$  state) and at 8 (to detect a  $10L$  state). The primary rf transitions occur at 6, and the rf regions at 5 and 7 are used to deplete and detect  $10L$  states not resolved by the laser, as described in the text. The  $n = 30$  atoms are detected by Stark ionization, with the resulting ions being deflected into a channeltron-electron multiplier at 9. Table I indicates the particular configuration used for all the transitions.

dielectric supports. Both ends of the line were connected to type- $N$  vacuum feedthroughs. The very abrupt change in geometry between the 50- $\Omega$  transmission line and the 50- $\Omega$  type- $N$  feedthrough was compensated for by carefully trimming the end of the inner conductor until the excess local capacitance was removed and the reflections minimized. The total reflections introduced by inserting the rf region into a matched 50- $\Omega$  line were measured as a function of frequency with a VSWR bridge and slotted line. After careful trimming, the total reflections were reduced to  $|\Gamma| < 0.05$  for the frequencies used in the present measurements. (Here  $\Gamma$  is the ratio of the electric field in the reflected wave to the electric field in the incident wave.) The dependence of the reflections on frequency showed indications of the excess capacitances at the ten dielectric supports, and a small impedance mismatch for the 3-m length of the region.

It was very important that the dc electric and magnetic fields inside of the rf region be small, since electric fields as small as 10 mV/cm (or transverse magnetic fields of 10 mG which lead to "motional" electric fields) shift the measured resonances by as much as 5 kHz. The magnet-

ic field was minimized by constructing the entire region out of nonmagnetic materials and by shielding the Earth's magnetic field using a  $\mu$ -metal shield. The shield was 6.5 in. in diameter and 140 in. long and was very successful in reducing the Earth's field, giving transverse fields of 2 mG or less at each point along its 3-m length, and axial fields of 2 mG or less along most of the region's length. In previous measurements, electric fields of 100 mV/cm or more were observed to build up with approximately a 10-h time constant [4]. These fields were apparently due to collection of charged particles on nominally conducting surfaces. The first step in reducing these fields was to carefully collimate the beam so that it could not strike any surface in the rf region. The inside of the region was carefully cleaned to remove nonconducting residues on which charges could accumulate. A final step in discouraging the charge buildup was to wrap the outer surface of the rf region with heating tape and

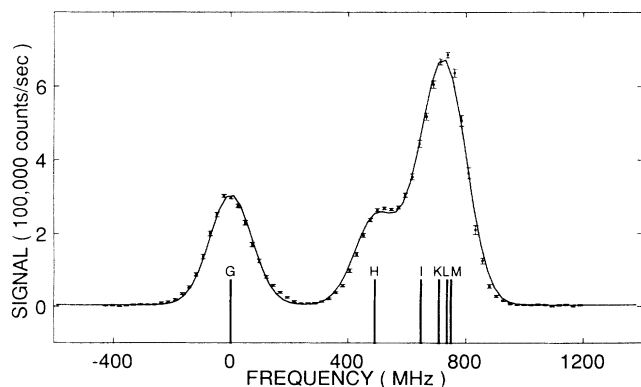


FIG. 3. A typical  $\text{CO}_2$   $n = 10$ -30 laser spectrum. The spectrum is taken by Doppler tuning the  $\text{CO}_2$  laser by varying the angle of intersection between the laser and atomic beams. The figure shows that the well-resolved  $10G$ - $30H$  resonance and the partially resolved  $10H$ - $30I$  resonance. The higher- $L$  resonances are not well resolved, and thus these states cannot be selectively detected without the auxiliary rf regions at 5 and 7 of Fig. 2.

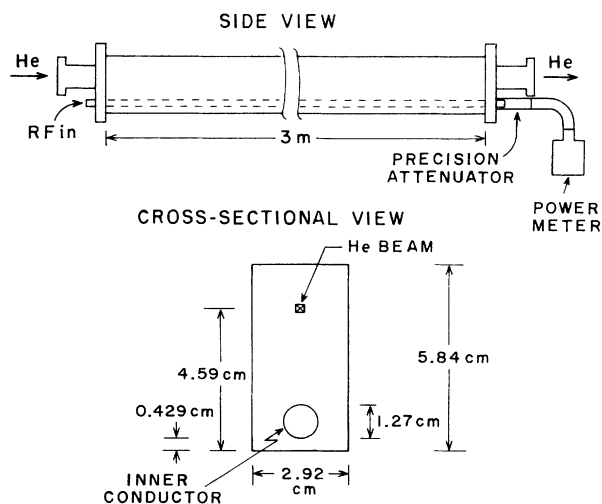


FIG. 4. The main rf interaction region. The region is a 3-m-long 50- $\Omega$  TEM transmission line constructed from copper WR229 waveguide as an outer conductor and a  $\frac{1}{2}$ -inch cylindrical inner conductor. The atomic beam travels parallel (or antiparallel) to the rf propagation direction. The rf electric-field direction is vertical at the center of the helium beam.

keep the region at 60°C during the measurements. This was accomplished using a slow feedback loop which heated only in the time period between measurements, to prevent possible problems due to magnetic fields from the heater currents. The heating caused a dramatic reduction in the size of the stray field, presumably because it kept nonconducting pump oils from accumulating on the surfaces. In a recent measurement [6], in which the region was also heated, residual electric fields which were about 10 mV/cm and very constant in magnitude over the length of the region were still observed. These fields were apparently due to contact potential differences between the inner and outer conductors, which were made from different metals. The present rf region was made with both of these conductors being copper.

The Stark-ionization and detection geometry, as well as typical operating voltages, are shown in Fig. 5. The atoms enter the region through a small ( $0.25 \times 0.50$  in.<sup>2</sup>) hole. The high- $n$  atoms have their outer electrons stripped in the 2000-V/cm field near the first stripping plate. The plate is at a potential of +4500 V and so the ions created here have an energy of 4.5 keV greater than the neutral beam. This difference in energy makes it easy to resolve the ions created at the stripping plate from atoms created elsewhere along the beam line or elsewhere in the detection region. The deflector plates spatially resolve ions of different energies, and were set to focus the ions created at the 4500-V stripping plate onto the channel electron multiplier. Horizontal deflection plates were used to further direct and focus these ions. Since the number of background ions collected was proportional to the pressure near the Stark-ionization plates, an attempt was made to reduce the pressure in the detection region to a few times  $10^{-8}$  Torr. At this pressure, the

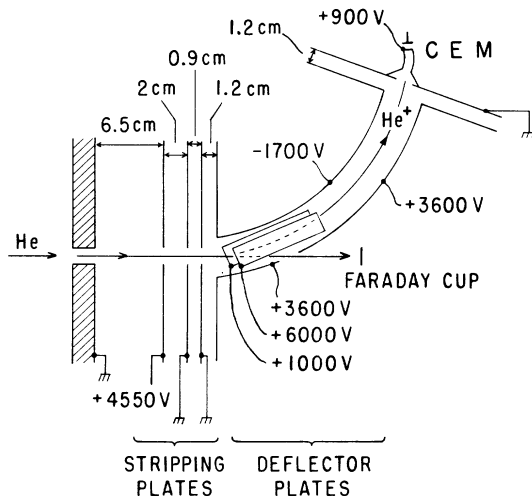


FIG. 5. The Stark-ionization detector. The atomic beam enters the high-vacuum region through a small opening and most of it propagates directly to a Faraday cup. The highest- $n$  states, however, are Stark ionized by a field of about 2000 V/cm near the 4550-V plate. The voltages of the deflectors is set so that only ions created near this 4550-V plate are deflected into the channeltron-electron multiplier (EM).

number of background ions was always smaller than the number of ions which resulted from the laser excitation up to  $n = 30$ .

### III. MEASUREMENTS

The 16 intervals measured in the present experiment are listed, along with the scheme used to measure them, in Table I. The data were taken in three independent data runs, each of which consisted of approximately 100 h of data-collection time. During each run, each of the 16 resonances was measured in each of the four possible orientations of the rf interaction region and of the rf propagation direction relative to the direction of the beam, as indicated in Table II. The average of measured line centers in these four configurations is nearly independent of Doppler shift and effects due to rf reflections, as discussed below.

The 16 intervals were scanned individually, with each scan consisting of about one hundred 30-sec measurements at a set of frequencies within 0.6 MHz of the center of the resonance. About two-thirds of the measurements were taken at frequencies near the half maximum points of the resonance being studied. Care was taken in ordering the measurements in a symmetric fashion so that any slow variations in signal size would not effect the line center. The exact set of points was modified for each run. The total time for an entire scan was very nearly 1 h. Measurements of the electric field were interspersed among these resonance scans as discussed below.

#### A. Shape and width of the resonances

Before we consider the line centers obtained from the scans, we will look at the shapes of the observed resonances. Line-shape data provide a check on the conditions inside the rf interaction region. In addition, accurate predictions of the line shape far from resonance are important in correcting for overlap of neighboring resonances. The best determination of the shape of the resonances is obtained by averaging all of the resonance scans of a particular interval. The averages of scans for 10G-H, H-I, I-K, and K-L measurements are shown in Fig. 6.

The expected line shape is that which results from an rf field of amplitude  $E$  which interacts with the atoms for a time  $T$ , namely,

$$S(\nu) = C \sum_m \left[ \frac{\sin(\pi b T)}{b} \right]^2 V_m^2, \quad (3)$$

where

$$b = [(2V_m)^2 + (\nu - \nu_0)^2]^{1/2}, \quad (4)$$

$$V_m = \frac{eE}{2h} \langle 10L, J', m_J | z | 10(L+1), J, m_J \rangle, \quad (5)$$

$\nu$  is the frequency at which the signal  $S$  is observed,  $C$  is a parameter which gives the height of the resonance, and  $\nu_0$  is the line center. The dependence of  $V$  on  $m_J$  has very little effect on the line shape, and so to a very good approximation

TABLE I. Settings for the observation of the 16 measured intervals and the two intervals which were used to study the stray electric fields.

Measured interval	First laser transition (4 of Fig. 2)	Auxiliary rf pump transitions (5 and 7 of Fig. 2)	Second laser transition (8 of Fig. 2)
$10^+G_4-10^+H_5$	10G-30H		10H-30I
$10^3G_3-10^3H_4$	10G-30H		10H-30I
$10^3G_5-10^3H_6$	10G-30H		10H-30I
$10^-G_4-10^-H_5$	10G-30H		10H-30I
$10^+H_5-10^+I_6$	10H-30I		10H-30I
$10^3H_4-10^3I_5$	10H-30I		10H-30I
$10^3H_6-10^3I_7$	10H-30I		10H-30I
$10^-H_5-10^-I_6$	10H-30I		10H-30I
$10^+I_6-10^+K_7$	10H-30I	$10^+H_5-10^+I_6$	10H-30I
$10^3I_5-10^3K_6$	10H-30I	$10^3H_4-10^3I_5$	10H-30I
$10^3I_7-10^3K_8$	10H-30I	$10^3H_6-10^3I_7$	10H-30I
$10^-I_6-10^-K_7$	10H-30I	$10^-H_5-10^-I_6$	10H-30I
$10^+K_7-10^+L_8$	10H-30I	$10^+H_5-10^+K_7$ (two photon)	10H-30I
$10^3K_6-10^3L_7$	10H-30I	$10^3H_4-10^3K_6$ (two photon)	10H-30I
$10^3K_8-10^3L_9$	10H-30I	$10^3H_6-10^3K_8$ (two photon)	10H-30I
$10^-K_7-10^-L_8$	10H-30I	$10^-H_5-10^-K_7$ (two photon)	10H-30I
$10^3K_8-10^3M_{10}$	10H-30I	$10^3H_6-10^3K_8$ (two photon)	10H-30I
$28^3D_3-10^3F_4$	$10^3P-28^3D$		$10^3P-28^3D$

$$S(\nu) = C \left[ \frac{\sin(\pi b T)}{b} \right]^2 V^2, \quad (6)$$

where  $V$  is an average of the  $V_m$ 's. The 3-m length of the rf-interaction region implies a time of  $T = 3.75 \mu\text{s}$ . Since the rf power for the transitions was chosen to maximize the signal, we would expect to have  $bT/2$  approximately equal to  $\pi/2$  for  $\nu = \nu_0$ , or  $V$  approximately equal to  $1/(4T) = 0.067 \text{ MHz}$ .  $V$  can be obtained more directly by using the calculated dipole matrix elements and the rf amplitude inferred from the rf power in the main rf region, as discussed below. Using this method, we find that  $V = 0.060(5) \text{ MHz}$  is appropriate for all of the 16 measured intervals.

The averaged scans are fit very poorly by  $S(\nu)$  of Eq. (6), as can be seen from the dashed lines in Fig. 6. The fit of the data near the wings of the resonance is very poor,

but the most serious discrepancy from the expected shape is that the resonances are about 10% broader than predicted. All of the 10G-H peaks show a width which is  $15 \pm 1\%$  broader than expected, while the 10H-I, I-K, and K-L are  $7 \pm 1\%$ ,  $7 \pm 1\%$ , and  $10 \pm 1\%$  broader, respectively.

There are many possible reasons for the observed broadening. The most obvious is radiative lifetime, which was not included in Eq. (6). The lifetimes of the 10G and 10H states, for example, are 1.81 and 2.75  $\mu\text{s}$ , which correspond to  $\Gamma$ 's of 88 and 58 kHz, respectively. However, it is the difference of these  $\Gamma$ 's (of 30 kHz) which contributes to the width of the resonance, and this only by adding approximately in quadrature with the 250-kHz transit width. In time-dependent perturbation theory the two-level shape (including lifetimes) is given by

TABLE II. The four configurations of propagation direction and rf region orientation used for the measurements. The final column shows the predicted energy position including the effects of first-order Doppler shifts and effects due to rf reflections.

Notation	Relative direction rf and helium beam	Orientation of rf region	Prediction of model for center
A	counterpropagating	end 1 near ion source	$\nu_0(1 - \beta - \epsilon_1)$
B	copropagating	end 1 near ion source	$\nu_0(1 + \beta + \epsilon_2)$
C	copropagating	end 2 near ion source	$\nu_0(1 + \beta + \epsilon_1)$
D	counterpropagating	end 2 near ion source	$\nu_0(1 - \beta - \epsilon_2)$

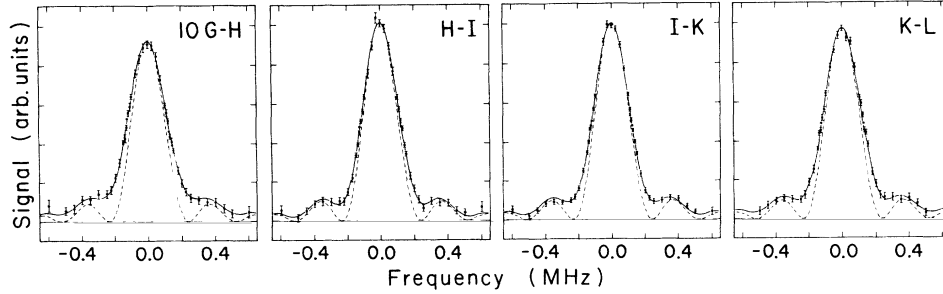


FIG. 6. The observed line shapes for 10G-H, 10H-I, 10I-K, and 10K-L resonances. The plotted points are the average of all data taken for each of the electric-fine-structure intervals. (The scans were adjusted to give a center frequency of zero and then averaged.) The observed shape is poorly fit by and somewhat broader than the simple two-level line shape of Eq. (6) shown as dashed lines. The data are, however, fit very well by the line shape of Eq. (9) which includes effects of radiative and blackbody-induced population transfers and is shown here as solid curves.

$$4V^2 \frac{e^{-2\gamma T} - 2e^{-\gamma T} \cos(\delta T) + 1}{\gamma^2 + \delta^2}, \quad (7)$$

where  $\delta = 2\pi(f_i - f_f - f)$  and  $\gamma = (1/\tau_i - 1/\tau_f)/2$ . Even for the 10G-to-10H transition, where the effect is largest, this shape is only 0.3% broadened by lifetimes. The same conclusion can also be reached using the full line shape of Eq. (6) rather than using time-dependent perturbation theory.

A second possible broadening mechanism is the presence of magnetic fields in the rf interaction region. These fields have the effect of splitting the  $\Delta m = +1$  and  $-1$  transitions by 2.8 MHz/G [15]. Thus the effect gives a line shape of

$$S(\nu - (1.4 \text{ MHz/G})B) + S(\nu + (1.4 \text{ MHz/G})B),$$

where  $S(\nu)$  is as given by Eq. (6). However, for the measured magnetic field of 2 mG, the broadening is only 0.04%.

Stark shifts, which shift the different  $m$  states by different amounts, also contribute to the width, but using the calculated matrix elements and the observed electric field (of about 4 mV/cm), the contribution is estimated to be less than 0.1% of the width. The variation in beam speed also contributes less than 0.1% if it is assumed that the kinetic energies vary by about 10 eV. The effects of the rf reflections on the line shape and the effect of overlapping peaks are discussed below and are also much too small to explain the width anomaly.

Another possible broadening mechanism is due to the nonideal shape of the rf field. The theoretical shape  $S(\nu)$  of Eq. (6) assumes that the field turns on instantly at a time  $t = 0$  and is constant in magnitude until it turns off instantly at a time  $t = T$ . While this is a fairly good approximation for the shape of the 3-m-long field, there are several possible imperfections in the field shape. The first concerns the fields at the entrance and exit of the region. The field will not remain constant over the last few centimeters or so of the region due to the fact that the shape of the inner conductor changes and due to the grounded plane at the rf feedthrough. The shape of the field in this region has been modeled using a three-dimensional relax-

ation method for a similar rf interaction region, and it was found that the effects of the ends (at least for dc fields) are confined to about 1 cm from the end of the region. An effective shortening of the region by 1 cm at each end would lead to only a 0.8% broadening. Nonidealities in the rf field shape can also result from bowing of the rf interaction region. The field shape is fairly sensitive to such bowing, since a 1-mm change in the relative positions of the beam and the inner conductor of the rf region leads to a 10% change in the rf field strength. Before assembling the beam line the rf region was checked (at room temperature) for bowing and was found to be straight to within 0.5 mm. However, during the runs the region was heated to 60°C, and this could lead to a bowing of the region. The resulting line shape can be obtained by treating the variation from the ideal line shape in time-dependent perturbation theory, and is particularly simple if it is assumed that the field shape is

$$E = E_0[1 + \epsilon \sin(\pi t / 3.75 \mu\text{s})] \quad \text{for } 0 < t < T.$$

The line shape that results is

$$4V^2 \left[ \frac{\sin^2(\pi b T)}{b^2} + \epsilon \frac{\sin(\pi b T)}{b} \left[ \frac{\sin[\pi T(\Delta + 0.13 \text{ MHz})]}{\Delta + 0.13 \text{ MHz}} + \frac{\sin[\pi T(\Delta - 0.13 \text{ MHz})]}{\Delta - 0.13 \text{ MHz}} \right] \right], \quad (8)$$

where  $b$  is given in Eq. (4). There are two reasons why this bowing effect does not appear to be the primary reason for the broadened line shape. The first is that the effect would be identical for all of the measured intervals, whereas we observe a variety of widths for the different  $L$  intervals. Second, the line shape of Eq. (8) fits the observed line shape very poorly, particularly at the wings of the resonances.

Collisions between the  $n = 10$  atoms and the back-

ground gas in the rf interaction region could also lead to broadening. The vacuum in this region was measured to be  $1 \times 10^{-7}$  Torr, using ion gauges at either end of the region. To test for any such collision effects, the pressure in the rf region was increased using a controlled leak at the center of the region. A 10G-to-*H* rf resonance scan was taken at pressures of  $6 \times 10^{-6}$  and  $4 \times 10^{-5}$  Torr. Even at these high pressures, the resonance was not observed to broaden (with the highest pressure resonance being  $5 \pm 7\%$  narrower than the resonance at  $10^{-7}$  Torr). If one assumes the broadening is proportional to pressure, this would indicate that there is less than 0.01% pressure broadening at  $10^{-7}$  Torr.

Another possible explanation of the broadened line shape is due to repopulation of the  $n = 10$  states within the rf interaction region. This repopulation could, for instance, be due to radiative decay of higher energy states and leads to a broadening since the interaction time for the states obtained by repopulation would be less than the full  $3.75\text{-}\mu\text{s}$  interaction time. For an  $nL$  to  $nL'$  transition, if one assumes that there is an original population difference of  $(1 - \alpha)\Delta$  between the two states and that the states are being repopulated at a constant rate during the time spent in the 3-m rf region, with  $\alpha\Delta$  more atoms being repopulated into  $nL$  than into  $nL'$  during the time  $T$  in the rf region, then the resulting line shape is

$$(1 - \alpha)4V^2 \frac{\sin^2(\pi bT)}{b^2} e^{-\gamma T} + \alpha \frac{4V^2}{Tb^2} \left[ \frac{e^{-\gamma T}}{-2\gamma} - \frac{e^{-\gamma T}}{\gamma^2 + 4\pi^2 b^2} \right. \\ \left. \times \left[ \frac{-\gamma}{2} \cos(2\pi bT + \pi b \sin(2\pi bT)) + \frac{1}{2}\gamma - \frac{-\gamma/2}{\gamma^2 + 4\pi^2 b^2} \right] \right], \quad (9)$$

where

$$\gamma = (1/\tau_i + 1/\tau_f)/2,$$

and  $b$  and  $V$  are as given in Eqs. (4) and (5). Note that the shape depends on the lifetimes of the states and that cascades will have a larger effect for states with short lifetimes. The data were fit to this repopulation line shape and the resulting fits are shown as solid lines in Fig. 6. All the data are fit very well by this shape, with  $\chi_{\text{reduced}}^2 = 1.02, 1.00, 1.01,$  and  $0.96$  for the *G-H*, *H-I*, *I-K*, and *K-L* shapes. In addition, when  $T$  is allowed to float, the fit returns values which are consistent with the known interaction time of  $3.75 \mu\text{s}$  for each of the four curves. Also, if a constant offset is allowed to float, the fit gives offsets consistent with zero in each case. The residuals from these fits are shown in Fig. 7. From the figure, it can be seen that the residuals have an rms value of 0.5% and are perfectly consistent with zero (with a  $\chi_{\text{reduced}}^2$  of 1.00) and that there is no evidence for asymmetries in the residuals (the  $\chi_{\text{reduced}}^2$  for testing whether the residual at  $\nu_0 - \nu$  is equal to the residual at  $\nu_0 + \nu$  is 1.00). The  $\alpha$ 's given by the fits are 0.52(3), 0.41(5), 0.47(3), and 0.54(4), for the 10G-*H*, *H-I*, *I-K*, and *K-L* intervals, indicating that almost half of the population differences are due to repopulation within the rf interaction region.

There are two mechanisms which could repopulate the states, namely, radiative decays from higher-energy states and blackbody-radiation-induced transitions from nearby states. The first is very well known and gives a repopulation rate (of state  $A$  from a higher-energy state  $B$ ) of

$$\frac{4e^2}{3\hbar c^3} \omega_{AB}^3 \frac{L_{\text{max}}}{2L_A + 1} R_{AB}^2 P(B), \quad (10)$$

where  $\hbar\omega_{AB}$  is the energy difference between states  $A$  and

$B$ ,  $R_{AB}$  is the integral of  $r$  times the product of the radial wave functions,  $L_{\text{max}}$  is the maximum of  $L_A$  and  $L_B$ , and  $P(B)$  is the population of state  $B$ . The repopulation rate due to blackbody-radiation-induced transitions is similar [16],

$$\frac{4e^2}{3\hbar c^3} \omega_{AB}^3 \frac{L_{\text{max}}}{2L_A + 1} R_{AB}^2 \frac{1}{e^{\hbar\omega_{AB}/kT} - 1} P(B), \quad (11)$$

where  $T$  is the temperature and where both higher- and lower-energy states contribute. The blackbody effect

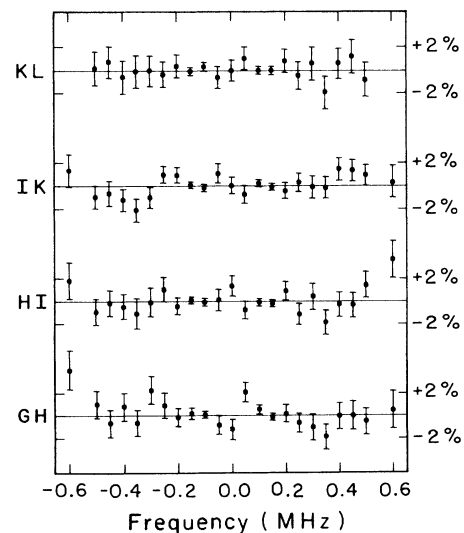


FIG. 7. The residuals from the fits of Fig. 6 normalized to the peak signal. The residuals from the fits are consistent with zero and reveal no obvious systematic pattern.

changes the lifetimes of these states (for  $T=350$  K) from 1.81, 2.75, 3.88, 5.21, and 6.72  $\mu\text{s}$  to 1.63, 2.29, 2.92, 3.43, and 3.81  $\mu\text{s}$  for the 10G, H, I, K, and L states, respectively. Both the radiative decay and blackbody transfer mechanisms contribute at about the same level for repopulation of the  $n=10$  states, with most of the radiative decays coming from the  $n=11, 12$ , and 13 states and most of the blackbody contribution coming from  $n=9$  and 11.

The total repopulation rate into a particular 10L state depends on the relative populations of all of the  $n, L$ , and  $m_L$  states entering the rf interaction region. These relative populations are determined by the charge exchange at 2 in Fig. 2, as well as the very large electric field at 3 in Fig. 2. Since the distribution created by charge exchange is unknown, the relative populations are very uncertain and, as a result, the total repopulation rates cannot be calculated with high confidence. If one assumes that the total population in the  $n$  states scales as  $1/n^3$  and that all  $L$  and  $m_L$  states within a given  $n$  are equally populated, one finds a repopulation rate for 10G (at the start of the rf interaction region) of  $(0.5 \times 10^5 \text{ s}^{-1})N_0(10G)$ , whereas the 10H state is repopulated at almost twice the rate [or  $(0.9 \times 10^5 \text{ s}^{-1})N_0(10G)$ ], and the higher- $L$  states having rates of  $(1.4 \times 10^5 \text{ s}^{-1})N_0(10G)$ ,  $(2.1 \times 10^{-5} \text{ s}^{-1})N_0(10G)$ , and  $(2.9 \times 10^5 \text{ s}^{-1})N_0(10G)$ , respectively. Here  $N_0(10G)$  is the initial population of the 10G state after the gas target. Thus, in the 3.75  $\mu\text{s}$  time spent in the rf interaction region, the 10G-10H population difference due to repopulation is about 0.15 times the initial 10G population. To get agreement with the  $\alpha=0.52(3)$  from the line-shape fits, one must assume that upon entering the rf region the population difference between the 10G and 10H states was also 15%. This is somewhat smaller than the population difference one might expect after the laser depletion of the 10G state at 4 in Fig. 2. However, as already mentioned, the repopulation rates (as well as the initial population difference) are a strong function of the original distribution of  $n, L$ , and  $m_L$  states. Because of the uncertainty in this distribution, values of  $\alpha$  of about 0.5 seem possible. This, combined with the excellent fits of Fig. 6, appears to indicate that the broadening and line shape are probably due to population transfer due to radiative and blackbody transitions. This view of the transitions, which involves population transfers within the rf interaction region, is quite different than the simple two-level model represented by Eq. (6), but still gives a symmetric line shape.

### B. Line centers and time-dependent systematic effects

Each individual scan was fit to the line shape of Eq. (9) in order to extract the line center. Since data were taken near the half maximum points, and since right and left half maximum points were always taken in pairs, another approach to fitting the data is to obtain a center directly from such a pair of points using the formula

$$\nu_0 = (\nu_+ + \nu_-) / 2 + \frac{S(\nu_+) - S(\nu_-)}{2m}, \quad (12)$$

where  $\nu_{\pm}$  are the frequencies near half maximum,  $m$  is the slope at these frequencies, and  $S(\nu)$  are the observed signals. The advantage of this approach is that a value for the center is obtained every 60 sec of data collection, and thus it is very insensitive to any longer-term drifts in the atomic beam or other parts of the apparatus. For much of the time in which data was being taken, there were considerable drifts in the beam current and it was found that this method of fitting does give a better statistical fit to the data. For each 1-h line scan, there were approximately 30 half maximum pairs and thus 30 determinations of the center frequency. These 30 centers were averaged and the standard deviation of the average was taken as a statistical error for the scan. The centers obtained in this method were consistent with the centers obtained by fitting the resonances to the line shape of Eq. (9).

Centers were obtained from these fits for each of the 12 resonance scans taken of each of the 16 measured intervals. For example, the centers obtained for one of the 16 intervals (the  $10^{-1}G_4$  to  $10^{-1}H_5$ ) are shown in Table III. Before the 12 line centers can be averaged (and checked for consistency), two systematic corrections which vary in time must first be applied. The first is due to the variation (of up to 30 V out of 13 kV) of the accelerating potential which led to different Doppler shifts at different times. The accelerating voltage ( $V_{\text{acc}}$ ) was monitored with a precision digital voltmeter. A correction of

$$\frac{V_{\text{acc}} - 13.000 \text{ kV}}{2(13.000 \text{ kV})} \beta v_0$$

was included to correct the centers to the value which they would have had if the accelerating voltage had been held constant at 13.000 kV. Corrections of up to 2 kHz were applied for 10G-H scans (as shown in the third column of Table III), with smaller corrections being applied for the higher- $L$  intervals. Since half of the scans had positive Doppler shifts and half had negative, the corrections were of both signs and the average of the corrections is small.

The second time-dependent systematic correction is due to dc Stark shifts. As mentioned above, small stray electric fields due to charging of surfaces, motion of the atom in residual magnetic fields, and due to contact potentials are present in the rf interaction region. The size of these fields was monitored by measuring the position of the  $28^3D-F$  resonance at various times during the data collection. This  $n=28$  resonance shifts at a rate of  $-3800 \text{ MHz}/(\text{V}/\text{cm})^2$ , which is much faster than the  $-12, -15, -7$ , and  $+32 \text{ MHz}/(\text{V}/\text{cm})^2$  Stark-shift rates of the  $n=10$  G-to-H, H-to-I, I-to-K, and K-to-L intervals. A scan of the  $n=28$  resonance is shown in Fig. 8, and the Doppler-corrected position of the  $28^3D_3$ -to- $^3F_4$  resonance (peak  $d$  of Fig. 8) as a function of time is shown in Fig. 9. The top axis of that figure is at 730.790 MHz, which is the expected zero-field position, and the approximate rms electric field is indicated on the right axis. From the figure it is clear that the electric field sometimes increases with time, and thus at least this part of the electric field is likely due to charging of the surfaces. The

TABLE III. Fitted line centers and time-dependent corrections for the 12 observations of the  $10^{-}G_4$ -to- $^{-}H_5$  resonance. Values are in MHz and numbers in parentheses are one standard deviation errors.

Run no. and configuration (see Table II)	Results of fits	Accel. voltage correction	Stark-shift correction	Corrected centers (MHz)	
1	A	494.2373(14)	+0.0002(0)	+0.0004(0)	494.2379(14)
	B	496.8752(10)	-0.0002(0)	+0.0004(0)	496.8754(10)
	C	496.8726(13)	+0.0000(0)	+0.0003(0)	496.8729(13)
	D	494.2353(16)	-0.0001(0)	+0.0004(0)	494.2356(16)
2	A	494.2365(20)	-0.0015(0)	+0.0003(0)	494.2353(20)
	B	496.8741(28)	+0.0013(0)	+0.0003(0)	496.8757(28)
	C	496.8775(31)	+0.0011(0)	+0.0006(1)	496.8792(31)
	D	494.2366(38)	-0.0008(0)	+0.0004(0)	494.2362(38)
3	A	494.2375(22)	-0.0017(0)	+0.0003(0)	494.2361(22)
	B	496.8777(23)	+0.0015(0)	+0.0003(0)	496.8795(23)
	C	496.8724(26)	-0.0023(0)	+0.0003(1)	496.8704(26)
	D	494.2395(27)	-0.0023(0)	+0.0003(1)	494.2375(27)

minimum electric field seen was 4 mV/cm. This field is too large to be due to motional fields, since the observed magnetic field of less than 2 mG leads to a motional field of less than 2 mV/cm. The origin of this residual electric field is unknown. The correction due to Stark shifts is given by the shift of the  $n=28$  resonance (as read off of Fig. 9) times the ratio of the Stark-shift rate of the measured interval to the rate for the  $n=28$  interval. The average correction for each of the  $G$ -to- $H$  intervals is +0.4 kHz, and for higher  $L$  they are +0.4, +0.2, and -1.0 kHz for the  $H$ -to- $I$ ,  $I$ -to- $K$ , and  $K$ -to- $L$  intervals, respectively. For example, Table III gives the corrections for the  $10^{-}G_4$ -to- $^{-}H_5$  interval. The errors given there are the statistical errors which result from reading the  $n=28$  shift from Fig. 9 and do not include the systematic errors which result from the uncertainties in the Stark-

shift rates, the uncertainty in the zero-field position of the  $n=28$  resonance, and the uncertainty of the entire procedure for predicting the shifts. These systematic uncertainties will be treated later. The  $10^{-}G_4$ -to- $^{-}H_5$  line centers corrected for variations in the accelerating voltage and for Stark shifts are shown in the final column of Table III.

In a few cases, one additional correction had to be made to the fitted centers. For five scans (all of them  $I$ -to- $K$ ), the exit of the rf interaction region was not properly terminated, having only a 10-dB attenuator, and thus giving rf reflections of about 10%. To correct for the shifts which are caused by these reflections, scans with and without proper termination were taken back-to-back. The two scans were found to have centers which differed by 2.6(10) kHz, and this correction was applied to each of the five scans.

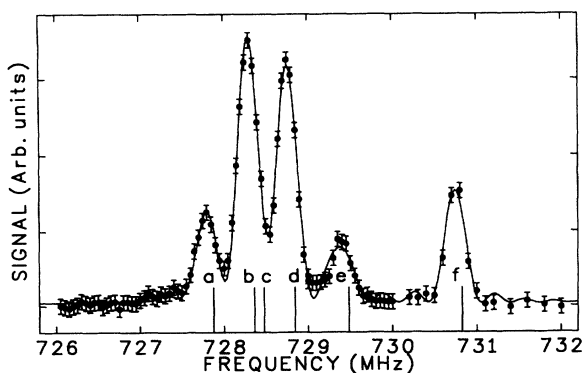


FIG. 8. A scan of the  $28^3D$ - $F$  resonances which were used for monitoring the stray electric field. The scan shown was taken with the rf and helium beam counterpropagating. The six resonances are as follows: (a)  $^3D_1$ - $^3F_2$ , (b)  $^3D_2$ - $^3F_3$ , (c)  $^3D_3$ - $^3F_3$ , (d)  $^3D_3$ - $^3F_4$ , (e)  $^3D_2$ - $^3F_2$ , and (f)  $^3D_2$ - $^3F_3$ . The vertical bars show the calculated peak positions in zero field. The slight downward shift indicates a stray field of about 5 mV/cm rms.

### C. Doppler-shift and reflected-rf corrections

Two of the systematic corrections, namely first-order Doppler shifts and rf-reflection shifts, cancel out when averaged over the four configurations listed in Table II. The centers should follow the pattern of  $\nu_0(1 \pm \beta)$  where the plus sign is to be used for configurations B and C (of Table II), in which the rf is propagating parallel to the helium beam. If effects due to rf reflections are included, there are small reflected waves as well as the forward traveling wave in the rf interaction region and this leads to a distortion of the line shape and a shift in the line center. The distortion is due to the fact that the reflected wave has the opposite sign of Doppler shift, and thus it is equivalent to having a second rf frequency present in the region. The sign of the effect depends on the sign of the Doppler shift, and thus the shift cancels when averaged over data taken with opposite Doppler shifts. In principle, the reflections may be different from the two ends of the rf region, and thus we use the notation  $\pm \epsilon_1 \nu_0$  and

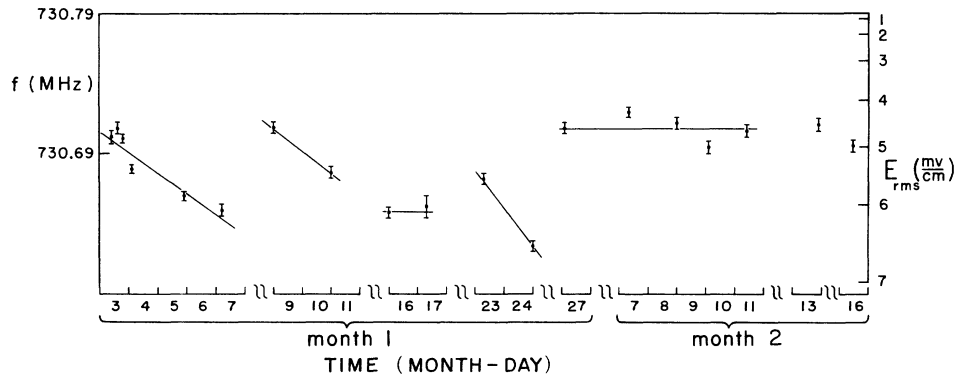


FIG. 9. The position of the  $28^3D_3\text{-}^3F_4$  resonance (corrected for Doppler shifts) during the time period of the data collection. The axis on the right shows the approximate electric field which can be inferred from the measured positions.

TABLE IV. Average fitted line centers and systematic corrections for the 16 measured  $n = 10$  intervals. Rows marked "average center" are averages of all scans of the line and include corrections for the time-dependent systematic effects. All values are in MHz and one standard deviation errors are given in parentheses.

	$^+L_L\text{-}^+(L+1)_{L+1}$	$^3L_{L-1}\text{-}^3(L+1)_L$	$^3L_{L+1}\text{-}^3(L+1)_{L+2}$	$^-L_L\text{-}^-(L+1)_{L+1}$
<b>10G-10H</b>				
Average center	486.860 74(73)	488.665 91(93)	491.965 27(66)	495.555 56(77)
Overlap of other peaks	-0.000 13(7)	0.000 21(11)	0.000 01(0)	0.000 00(0)
Systematics from Table VI	-0.001 92(32)	-0.001 93(32)	-0.001 94(32)	-0.001 96(32)
Total	486.858 69(79)	488.664 19(98)	491.963 34(73)	495.553 60(83)
<b>10H-10I</b>				
Average center	154.668 73(36)	155.815 23(44)	157.629 52(34)	159.648 55(42)
Overlap of other peaks	-0.000 13(7)	-0.000 07(7)	0.000 06(4)	0.000 10(5)
Systematics from Table VI	-0.000 76(13)	-0.000 77(13)	-0.000 78(13)	-0.000 79(13)
Total	154.667 84(39)	155.814 39(46)	157.628 80(36)	159.647 86(44)
<b>10I-10K</b>				
Average center	59.313 40(40)	60.087 25(45)	61.196 51(29)	62.431 90(38)
Overlap of other peaks	-0.000 36(18)	0.000 33(16)	0.000 01(0)	0.000 03(2)
Systematics from Table VI	-0.000 43(8)	-0.000 44(8)	-0.000 44(8)	-0.000 45(8)
Total	59.312 61(44)	60.087 14(48)	61.196 08(30)	62.431 48(39)
<b>10K-10L</b>				
Average center	26.167 99(51)	26.707 78(63)	27.438 57(50)	28.248 72(50)
Overlap of other peaks	-0.000 14(7)	0.000 78(38)	0.000 00(5)	0.000 12(6)
Systematics from Table VI	-0.000 29(31)	-0.000 29(31)	-0.000 30(31)	-0.000 30(31)
Total	26.167 56(60)	26.708 27(80)	27.438 26(59)	28.248 54(59)

$\pm\epsilon_2\nu_0$  for shifts from the two ends, as shown in Table II.

The unshifted center can be obtained by averaging  $\nu_A$  and  $\nu_C$  or  $\nu_B$  and  $\nu_D$ , and the effects of Doppler shifts and reflected waves can be obtained from the differences between these pairs of frequencies. More generally, all of the  $G$ -to- $H$  data can be fit to the model of Table II using a least-squares fit to obtain the best values of each of the four  $G$ -to- $H$  intervals, as well as values for  $\beta+\epsilon_1^{GH}$  and  $\beta+\epsilon_2^{GH}$ . The values for the centers obtained by such a fit (and similar fits for the  $H$ - $I$ ,  $I$ - $K$ , and  $K$ - $L$  centers) are given in Table IV, where they are labeled "average center." The values of  $\beta+\epsilon$  from the fits are listed in Table V. The  $\chi^2$  for these fits indicates how well the data fit the model and how consistent the measurements of the centers are. For the higher- $L$  intervals, the values of  $\chi_{\text{reduced}}^2$  are very reasonable (0.99 for the  $H$ - $I$ 's, 0.96 for the  $I$ - $K$ 's, and 1.36 for the  $K$ - $L$ 's). The consistency of the  $G$ -to- $H$  measurements, however, was quite poor, with  $\chi_{\text{reduced}}^2=2.16$ . Since the  $G$ -to- $H$  intervals are most sensitive to variations in beam speed, it may be that the measured accelerating potential was not a perfect measure of the beam speed since the potential at the point where the atoms are ionized in the source may not equal the potential at the point where it was measured by the voltmeter. This seems especially plausible since the source conditions changed considerably during the data collection. Variations in accelerating voltages of about 20 V could give the observed scatter in the data, and this variation seems well within what one might reasonably expect. To compensate for any error that these variations could cause, the errors of the line centers have been expanded by the square root of  $\chi_{\text{reduced}}^2$ .

The values of  $\beta+\epsilon$  obtained from the fits are listed in Table V. The  $\epsilon$ 's for the 10 $G$ - $H$  interval are expected to be extremely small. (This is because the Doppler shift is much larger than the linewidth for these resonances.) Thus the two values of  $\beta+\epsilon^{GH}$  are good estimates of  $\beta$  and we get  $\beta=0.002\,663\,3(8)$ , which implies an accelerating potential of 13.221 kV. This differs from the 13.000-kV reading by our Data Precision model D41A high-voltage probe with a Data Precision 3600 digital multimeter by a factor of 1.0170(4), which is reasonably consistent with the 1.020(1) calibration factor of the probe at 500 V.

This value of  $\beta$  can be subtracted from each of the  $\beta+\epsilon$ 's in Table V to obtain the  $\epsilon$ 's for each end of the region for the four electric-fine-structure (EFS) intervals. As can be seen from the fourth row of Table V, the  $\epsilon$ 's

from end 2 are all consistent with zero and thus with no reflection effects. The  $\epsilon$ 's from end 1 are small but nonzero. The shifts from these  $\epsilon$ 's are 1 kHz or less, and as mentioned above, the shifts cancel when data taken in the two rf propagation directions are averaged.

#### D. Overlap of neighboring resonances

There are small shifts due to the slight overlap of neighboring resonances. This overlap is small for the lower- $L$  resonances because the spacing between the resonances is large compared to the linewidth. For the higher- $L$  resonances the overlap is also small since the auxiliary rf regions select out a single resonance, making the neighboring peaks small. To determine the size of the neighboring resonances, one data point was taken during each scan at the center of each of the three other MFS components. For the  $G$ -to- $H$  and  $H$ -to- $I$  scans, the relative sizes of the four MFS components are consistent with the expected  $(2J+1)$  statistical weights. For the higher- $L$  transitions, the neighboring peaks are much smaller (0–25% of the main resonance) because of the selectivity of the auxiliary rf regions at 5 and 7 in Fig. 2. In some cases the settings of the auxiliary regions were changed for some of the scans. In order to correct for the overlap of resonances, it is necessary to know the shape at the wings of the resonances. To this end, the data shown in Fig. 10 were taken on the right side of the  $^{-}H_5$ -to- $^{-}I_6$  resonance, and fit to the line shape of Eq. (9). The line shape fits the data well ( $\chi_{\text{reduced}}^2=0.66$ ). The estimate of the shift due to overlap is given by

$$R = \frac{S(\Delta - 0.125 \text{ MHz}) - S(\Delta + 0.125 \text{ MHz})}{2(dS/d\nu)_{\text{at } \nu=0.125 \text{ MHz}}},$$

where  $R$  is the relative height of the neighboring peak,  $\Delta$  is the separation between the main resonance and its neighbor, and  $S(\nu-\nu_0)$  is given by Eq. (9). The shifts for each resonance and the uncertainty in the shift is given in Table IV. The 50% uncertainty comes from the uncertainties in the relative heights of the neighboring peaks and from the uncertainty of the line shape at the wings.

In addition to the four strongly allowed MFS components for each EFS interval, there are also several weakly allowed components and these components could, in principle, also shift the resonances. Fortunately, however, these resonances are sufficiently weak and sufficiently well spaced from the main resonances to give negligible effects (shifts of less than  $10^{-5}$  MHz).

TABLE V. Effects of rf reflections. The observed values for  $\beta+\epsilon$  and  $\epsilon$ . Numbers in parentheses represent one standard deviation errors.

	10G-H	10H-L	10I-K	10K-L
$\beta+\epsilon_1$	0.002 664(1)	0.002 665(2)	0.002 681(4)	0.002 632(13)
$\beta+\epsilon_2$	0.002 663(1)	0.002 662(2)	0.002 664(4)	0.002 649(15)
$\epsilon_1^a$	0.000 001(1)	0.000 002(2)	0.000 018(5)	-0.000 031(13)
$\epsilon_2^a$	-0.000 001(1)	-0.000 001(2)	0.000 000(5)	-0.000 014(16)

<sup>a</sup>A value of  $\beta=0.002\,663\,3(8)$  was used.

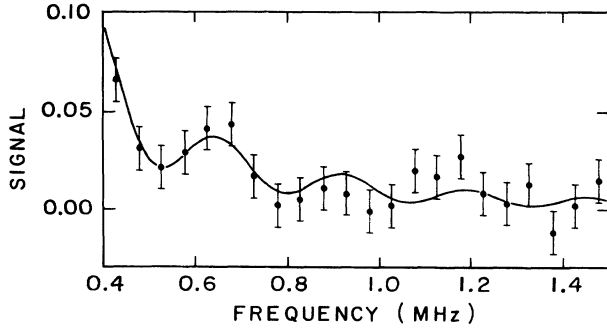


FIG. 10. The right wing of the  $10^{-}H_5$ -to- $^{-}I_6$  resonance, normalized to the peak signal. The data are fit well by the line shape of Eq. (9). The data were taken to determine the effects of overlap of neighboring resonances.

### E. Other systematic corrections

Several systematic corrections and uncertainties that must be added to the line centers are listed in Table VI. The first of these is due to second-order Doppler shifts. As discussed above, the data were taken with the rf propagating in the direction of and counter to the direction in which the atoms were traveling. The frequencies  $\nu_{\text{lab}}^{\text{co}}$  and  $\nu_{\text{lab}}^{\text{counter}}$  required in the laboratory for the atoms to encounter a frequency  $\nu_0$  (including time dilation) are

$$\nu_{\text{lab}}^{\text{co}} = \nu_0 [1 + \beta + \frac{1}{2}\beta^2 + O(\beta^3)]$$

and

$$\nu_{\text{lab}}^{\text{counter}} = \nu_0 [1 - \beta + \frac{1}{2}\beta^2 + O(\beta^3)] .$$

Taking the average of these gives

$$\frac{1}{2}(\nu_{\text{lab}}^{\text{co}} + \nu_{\text{lab}}^{\text{counter}}) = \nu_0 + \frac{1}{2}\beta^2\nu_0 + O(\beta^3) .$$

Thus (to order  $\beta^2$ ) we must apply a correction of  $-\frac{1}{2}\beta^2\nu_0$  to the average of the co- and counterpropagating frequencies. (This is in contrast to the case in which the rf propagation is at  $90^\circ$  to the atomic velocity, in which case  $\nu_{\text{lab}} = \nu_0 - \frac{1}{2}\beta^2\nu_0$  and the correction is  $+\frac{1}{2}\beta^2\nu_0$ .) The uncertainty associated with this correction is very small.

The second correction is due to blackbody radiation, which induces ac Stark shifts in the states. These shifts

have been calculated by Farley and Wing [16], and using their prescriptions, the contributions of 330 K blackbody shift to the  $10G-H$ ,  $H-I$ ,  $I-K$ , and  $K-L$  intervals is  $+0.19(3)$ ,  $+0.20(3)$ ,  $+0.18(3)$ , and  $+0.16(3)$  kHz, where the uncertainty is primarily due to the  $15^\circ\text{C}$  uncertainty in the temperature of the rf region.

As discussed above, most of the data points were taken near the half maximum points, and thus the centers are derived from the data using the formula

$$\nu_0 = (\nu_+ + \nu_-) / 2 + \frac{S(\nu_+) - S(\nu_-)}{2m} ,$$

where  $\nu_{\pm}$  are the frequencies near half maximum,  $m$  is the slope at these frequencies, and  $S(\nu)$  are the observed signals. Note that if  $\nu_+$  and  $\nu_-$  are chosen symmetrically around the line center, then the average contribution of the second term is zero and the average  $\nu_0$  obtained is insensitive to the slope  $m$  which is used. If, however,  $\nu_+$  and  $\nu_-$  are not symmetric about the line center, the result does depend on the choice of  $m$ , and any uncertainty in the value of  $m$  leads to an uncertainty in the value of the line center. For the case of the  $H$ -to- $I$ ,  $I$ -to- $K$ , and  $K$ -to- $L$  resonances, the points chosen were close enough to symmetric to give no significant error. However, in the case of the  $G$ -to- $H$  resonances, the points were approximately 7 kHz off symmetrical, and thus the uncertainty in the slope leads to an uncertainty in the intervals. These uncertainties are given in Table VI.

The next systematic correction is due to ac Stark shifts. These shifts are due to the ac electric field of the rf which is driving the transition. A state  $a$  is shifted by

$$\sum_k \left[ \frac{V_{ak}^2}{E_a - E_k + \nu} + \frac{V_{ak}^2}{E_a - E_k - \nu} \right] , \quad (13)$$

where  $V$  is the matrix element of  $eE_{\text{rf}}z/2h$ , and the sum is over all states  $k$  which have nonzero matrix elements. If  $\nu$  is set to the frequency  $E_b - E_a$ , then the first term becomes infinite for  $b=k$ . This term is excluded from the sum (it is the resonance term which leads to the rf transition) and the second term (customarily referred to as the Bloch-Seigert shift) is still included. Only the states  $k$  which are in  $n=10$  give significant contributions, since the energy denominators get large for other  $n$ 's. The shift is a function of  $m_j$  since the matrix elements  $V$  depend on

TABLE VI. Some systematic corrections and uncertainties for the measured intervals. All values are in kHz, and numbers in parentheses represent one standard deviation errors.

	10G-H	10H-I	10I-K	10K-L
Second-order Doppler shift	-1.74(0)	-0.56(0)	-0.21(0)	-0.09(0)
Blackbody shifts	-0.19(3)	-0.20(3)	-0.18(3)	-0.16(3)
Uncertainties in slope				
at $\frac{1}{2}$ -max	0.00(29)	0.00(0)	0.00(0)	0.00(0)
ac Stark shift	-0.01(0)	-0.02(0)	-0.04(0)	-0.04(0)
rf power variations	0.00(2)	0.00(2)	0.00(2)	0.00(2)
Pressure shifts	0.00(4)	0.00(4)	0.00(4)	0.00(4)
Uncertainties in Stark shift	0.00(12)	0.00(12)	0.00(7)	0.00(30)

$m_j$ , but for the very small shifts here we need not worry about that dependence. In all cases the shifts are positive for the energy intervals, and the corrections for these shifts are shown in Table VI.

Another uncertainty is due to possible variations in the field seen by the atoms as the frequency is adjusted. These variations could be due to rf reflections or attenuations in any of the rf components between the signal generator and the rf region. To obtain an estimate of the size of these variations, the rf power was measured at the exit of the rf region as a function of frequency. Variations of 0.2%/MHz or less were observed. These variations include possible variations in the rf power meter and rf elements at the exit of the rf region. For 0.2%/MHz variations, there is a difference of 0.01% in the signal sizes at the two half maximum points, and a shift of 10 Hz. To be conservative, the uncertainty due to this effect is taken to be 20 Hz, as shown in Table VI.

To determine whether there are shifts due to collisions with background gas in the rf region, the pressure in this region was increased, as described above. The 10G-H resonance was measured at pressures of  $1 \times 10^7$ ,  $6 \times 10^{-6}$ , and  $4 \times 10^{-5}$  Torr. The resonance was found to shift by 0.02(2) kHz/ $10^{-7}$  Torr, which is consistent with no pressure shift. An uncertainty of 0.04 kHz is included in Table VI to account for possible pressure shifts.

#### F. Stark shift uncertainty

There is one additional uncertainty in the intervals and it is due to the uncertainty in the Stark shifts of the states. The Stark-shift corrections are already included in the time-dependent systematic corrections (as illustrated in Table III), but the uncertainties in the shifts are not included. As mentioned above, the size of the stray electric fields was monitored by measuring the position of the  $28^3D-F$  resonance at various times during the data collection. This  $n=28$  resonance shifts at a rate of  $-3800$  MHz/(V/cm)<sup>2</sup>, which is much faster than the  $-12$ ,  $-15$ ,  $-7$ , and  $+32$  MHz/(V/cm)<sup>2</sup> Stark-shift rates of the  $n=10$  G-to-H, H-to-I, I-to-K, and K-to-L intervals. The position of the  $28^3D_3$ -to- $^3F_4$  resonance (which, as we discuss below, is estimated to be 730.790 MHz in zero field) as a function of time can be read from Fig. 9. The correction due to Stark shifts is given by the shift of the  $n=28$  resonance relative to the expected position times the ratio of the Stark-shift rate of the measured interval to the rate for the  $n=28$  interval. There are several sources of systematic error in this process of determining the Stark-shift correction, namely (a) the uncertainty in the zero-field position of the  $n=28$  resonance, (b) the uncertainty in the Stark-shift rates of the  $n=10$  and 28 resonances, and (c) the reliability of using  $n=28$  resonances for determining the stray electric field. The first two lead to small uncertainties, as discussed in the next two paragraphs. The third is related to the fact that the  $n=28$  shift rate is so large that for certain types of stray fields the observed shift may not be quadratic in  $E$ .

Although no direct experimental values are available for the zero-field position of the  $28^3D-F$  resonances, their positions can be obtained by extrapolating the ex-

perimental values at lower  $n$ 's, and this has been done by Farley, MacAdam, and Wing [17]. However, the uncertainties of their extrapolated values are too large to be useful here. There also have been no direct calculations for the position of these states but, once again, one can obtain estimates by extrapolating calculated energies at lower  $n$ 's. Fortunately, these lower- $n$  energies have been calculated very accurately by Drake [18,19]. These lower- $n$  calculations agree with the experimental values of Farley, MacAdam, and Wing [17] to within a few parts per million (ppm). The lower- $n$  calculations can be extrapolated up to  $n=28$  and they give  $\nu_{28}=730.790(2)$  MHz for the  $28^3D_3-^3F_4$  resonance shown in Fig. 9. The quoted error includes uncertainties from the extrapolation as well as a 3 ppm uncertainty from the comparison between theory and experiment at lower  $L$ . The uncertainty in  $\nu_{28}$  lead to negligible errors in the determination of the  $n=10$  Stark shifts.

The Stark-shift rate for the  $28^3D-F$  resonances is  $-3800(200)$  MHz/(V/cm)<sup>2</sup>. The uncertainty results from slightly different rates for different values of  $J$  and  $m_j$ . The shift rates for the  $n=10$  resonances also depend on  $m$  and thus the average rate depends on the  $m$ -state populations and also on the relative strengths of the transitions for different  $m$ 's. These strengths are approximately independent of  $m$  since all of the  $m$ 's are near saturation. Although the relative populations of the  $m$  levels is not known, the relative heights of the MFS components for the G-to-H and H-to-I measurements give a strong indication that the  $m$  states are approximately equally populated. For the I-to-K and K-to-L resonances, the lower- $m$  states are likely favored since only states which connect to 10H states are transferred to the 10H state by the post-pump region and are detected. With these considerations in mind, the average Stark-shift rates of  $-12(1)$ ,  $-15(2)$ ,  $-7(1)$ , and  $+32(3)$  are used, and thus lead to approximately 10% uncertainties in the (small) Stark-shift corrections.

The final uncertainty in the Stark shift is due to the possible problems in the entire procedure. For example it is known that large fields which act for a short time duration (i.e., are localized in a particular position in the rf interaction) do not shift the  $n=28$  resonances proportionally to the square of the rms field, as would be naively expected. This effect occurs when the electric field is sufficiently large to shift the  $n=28$  resonance by much more than its linewidth. For example if the electric field is such that the  $n=28$  resonance is shifted by 1 MHz for one-tenth of the 3.75- $\mu$ s interaction time and is unshifted for the remainder of the time, the expected line shape would be a slightly broadened resonance at the unshifted position, and a much smaller (about 1%) and much broader (about ten times as broad) resonance 1 MHz below the main resonance. The presence of these lower-frequency shoulders has been observed in previous measurements [6], and shifts which were not proportional to the square of the rms fields were observed in preliminary measurements in which localized fields were present due to the accidental presence of ferromagnetic materials near the rf region. Even though the  $n=28$  resonances taken in the current data runs were free of any such

shoulder (see Fig. 8), it was still important to establish the appropriateness of the  $n = 28$  method of determining the fields. To do this, we took measurements of another resonance, namely the two-photon  $10^3K_8 - 10^3M_{10}$  which shifts more quickly than the 16 main intervals, but 20 times more slowly than the  $n = 28$  resonance and is thus much less subject to the effects described above. Measurements of this interval were interspersed throughout the data runs. These lines were fit to give the line centers, and the average of all of the observations is 41.2740(19) MHz. This cannot be compared to the zero-field value of 41.248 9(3) (which comes from the calculations of Drachman [1] and Martinis and Pilkuhn [20]) until the experimental numbers are corrected for ac Stark shifts.

There are several ways to obtain this ac Stark shift, the most obvious is to take data at different powers and extrapolate back to zero power. Using this method we get a shift of 0.020(5) MHz. From the saturation behavior of the  $K$ -to- $M$  resonance, it is possible to determine that the rf field amplitude is  $E_{rf} = 0.0225(3)$  V/cm. This estimate of the field size agrees with other measures of the field amplitude, and can be combined with the calculated ac Stark-shift rates to give a second and more accurate estimate of the ac shift of 0.018 2(6) MHz.

Correcting our measured  $10^3K_8 - 10^3M_{10}$  frequency by this ac shift gives a measured  $10K-M$  which is  $6.9 \pm 2.0$  kHz larger than the calculated position. Using the calculated dc Stark-shift rate of  $154$  MHz/(V/cm)<sup>2</sup>, this indicates that there was an rms field of  $6.7 \pm 0.9$  mV/cm during the time of the  $10K-M$  scans. Using the  $n = 28$  resonance and Fig. 9 gives an rms field for the same times of  $5.6 \pm 0.1$  mV/cm. The level of agreement between these two methods for determining the stray field indicate that the Stark shifts predicted from the  $n = 28$  resonance are reliable to at least 30%. Thus an error of 30% of the entire Stark shift is included in the uncertainties given in Table VI.

As another check on our electric-field diagnostic, we monitored the position of the  $28^3D-F$  resonances as we applied an electrostatic potential on the inner conductor of the rf interaction region. The resulting centers (for the  $28^3D_3 - 3F_4$ ) are shown in Fig. 11. This figure verifies the expected quadratic shift of the resonances and gives a least-squares fit of

$$730.702(7) \text{ MHz} + \left[ 0.87(7) \frac{\text{MHz}}{\text{V}} \right] V_{\text{applied}} - \left[ 18.2(8) \frac{\text{MHz}}{\text{V}^2} \right] V_{\text{applied}}^2 \quad (14)$$

The 730.702(7) MHz constant indicates that the resonance is shifted by  $-0.088$  MHz from its expected position of 730.790 MHz when no potential is applied and thus that there is an rms stray electric field of about 4.8 mV/cm present. If we add an applied field to this stray field we expect the  $n = 28$  resonance center to be

$$730.790 \text{ MHz} + k_{28D-F} (E_{\text{stray}} + E_{\text{applied}})_{\text{rms}}^2,$$

where  $k_{28D-F} = -3800(200)$  MHz/(V/cm)<sup>2</sup> is the dc shift

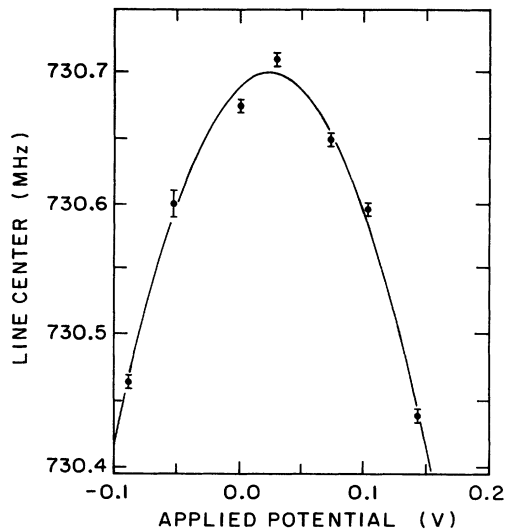


FIG. 11. The position of the  $28^3D_3 - 3F_4$  resonance (corrected for Doppler shifts) as a function of voltage applied to the inner conductor of the rf region. The resonance shows the expected quadratic shift. The fact that the resonance shifts upward for small positive voltages indicates that part of the stray field inside the region is being canceled by the applied voltage.

rate of the  $28^3D-F$  resonance, and  $E_{\text{applied}}$  is the field which is seen at the atomic beam when the potential is applied to the inner conductor. This field clearly must be proportional to the potential  $V_{\text{applied}}$  and can be written as  $V_{\text{applied}}/d$ . The linear coefficient of  $0.87(7)$  MHz/V indicates that the applied potential is partially canceling the stray field present at zero potential. The  $-18.2(8)$  MHz/V<sup>2</sup> coefficient of  $V_{\text{inner cond}}^2$  is equal to the shift rate  $k_{28D-F}$  divided by the  $d^2$ , which gives  $d = 14.4$  cm if we use the known values of  $k_{28D-F}$ . This  $d$ , along with the  $V$  obtained from the rf power,

$$\mathcal{P}_{\text{rf}} = 0.5 \text{ V}^2 / 50 \Omega,$$

gives values of rf electric-field amplitudes which are consistent with those obtained from the saturation behavior of the resonances.

The totals of the fitted centers plus all of the corrections are given in Table IV. These are the final experimental values for the 16 intervals measured in this experiment.

#### IV. DISCUSSION OF RESULTS

The final results for the  $n = 10$  measurements are given in Table VII, along with previous  $n = 10$  measurements. The four results for each  $10L-10(L+1)$  interval can be combined to give a value for the interval between the mean energies for each  $L$ . The mean energy is the statistically weighted average of the energies of the four magnetic fine-structure states, i.e.,

TABLE VII. Final measured values for the 16  $n = 10$  intervals. The measurements are compared to previous measurements where applicable. The previous measurements for the  $10D-F$  come from Ref. [17], for  $10F-G$  and  $10G-H$  come from Ref. [6], and for higher  $L$  come from Ref. [5]. The mean energy intervals are also given and these are calculated using Eq. (6) of Ref. [6]. The measurements are compared to the theory of Drake [2,19]. All values are in MHz with one standard deviation errors given in parentheses.

$n = 10$ interval	Previous measurement	Present measurement	Theory (Drake)	Expt. minus theory
$^1D_2^-+F_3$	10 918.797(53)		10 918.817(2)	-0.020(53)
$^3D_1^-+F_2$	15 760.707(81)		15 760.684(2)	0.023(81)
$^3D_3^-+F_4$	15 782.101(74)		15 782.012(2)	0.089(74)
$^3D_2^-+F_3$	15 770.554(67)		15 770.682(2)	-0.128(67)
$D_{\text{mean}}-F_{\text{mean}}$	14 560.651(34)		14 560.653(2)	-0.002(34)
$^+F_3^-+G_4$	2 017.311 0(31)		2 017.325 3(3)	-0.014 3(31)
$^3F_2^-+G_3$	2 037.896 1(47)		2 037.910 8(3)	-0.014 7(47)
$^3F_4^-+G_5$	2 044.970 3(39)		2 044.988 6(3)	-0.018 3(39)
$^-F_3^-+G_4$	2 043.438 1(52)		2 043.451 0(3)	-0.012 9(52)
$F_{\text{mean}}-G_{\text{mean}}$	2 036.559 0(22)		2 036.574 2(3)	-0.015 2(22)
$^+G_4^-+H_5$	486.862 3(17)	486.858 69(79)	486.861 21(10)	-0.002 52(80)
$^3G_3^-+H_4$	488.668 6(20)	488.664 19(98)	488.666 25(10)	-0.002 06(99)
$^3G_5^-+H_6$	491.967 1(14)	491.963 34(73)	491.966 15(10)	-0.002 81(74)
$^-G_4^-+H_5$	495.557 1(17)	495.553 60(83)	495.557 78(10)	-0.004 18(84)
$G_{\text{mean}}-H_{\text{mean}}$	491.009 0(13)	491.005 23(49)	491.008 16(10)	-0.002 93(50)
$^+H_5^-+I_6$		154.667 84(39)	154.668 57(5)	-0.000 73(39)
$^3H_4^-+I_5$		155.814 39(46)	155.815 01(5)	-0.000 62(46)
$^3H_6^-+I_7$		157.628 80(36)	157.630 54(5)	-0.001 74(36)
$^-H_5^-+I_6$		159.647 86(44)	159.649 56(5)	-0.001 70(44)
$H_{\text{mean}}-I_{\text{mean}}$	157.050 8(26) <sup>a</sup>	157.052 41(23)	157.053 66(5)	-0.001 25(24)
$^+I_6^-+K_7$		59.312 61(44)	59.314 04(1)	-0.001 43(44)
$^3I_5^-+K_6$		60.087 14(48)	60.087 53(1)	-0.000 39(48)
$^3I_7^-+K_8$		61.196 08(30)	61.196 70(1)	-0.000 62(30)
$^-I_6^-+K_7$		62.431 48(39)	62.432 27(1)	-0.000 79(39)
$I_{\text{mean}}-K_{\text{mean}}$	60.815 2(18) <sup>a</sup>	60.815 95(20)	60.816 77(1)	-0.000 82(20)
$^+K_7^-+L_8$		26.167 56(60)		
$^3K_6^-+L_7$		26.708 27(80)		
$^3K_8^-+L_9$		27.438 26(59)		
$^-K_7^-+L_8$		28.248 54(59)		
$K_{\text{mean}}-L_{\text{mean}}$	27.183 5(63) <sup>a</sup>	27.174 72(52)		

<sup>a</sup>In these previous measurements, the numbers quoted were the so-called electric-fine-structure (EFS) intervals, which are defined in Ref. [5]. These are related to the mean intervals by  $E_{\text{mean}} = E_{\text{EFS}} - V_x/2$ . However, since the exchange energies are very small for these high- $L$  states, the difference between  $E_{\text{mean}}$  and  $E_{\text{EFS}}$  is less than 40 Hz.

$$E(L_{\text{mean}}) = \frac{1}{4L+4} [(2L+1)E(^+L_L) + (2L+1)E(^-L_L) \\ + (2L-1)E(^3L_{L-1}) + (2L+3)E(^3L_{L+1})].$$

The interval between the mean energies of  $10L$  and  $10(L+1)$  can be deduced from the four measured  $10L$ -to- $10(L+1)$  intervals [as described in Eq. (6) of Ref. [6]] using

$$E(L_{\text{mean}}) - E(L'_{\text{mean}}) = \frac{1}{4} \left[ \nu(^+L_L - ^+L'_{L'}) + \frac{2L'-1}{2L'+1} \nu(^3L_{L-1} - ^3L'_{L'-1}) + \frac{2L'+3}{2L'+1} \nu(^3L_{L+1} - ^3L'_{L'+1}) \right. \\ \left. + \nu(^-L_L - ^-L'_{L'}) \right] - \left[ \frac{1}{4L+2} - \frac{1}{4L'+2} \right] [E(^3L_{L-1}) - E(^3L_{L+1})].$$

The quantity  $E(^3L_{L-1}) - E(^3L_{L+1})$  must be obtained from theory or from other measurements. Notice that the coefficient of  $E(^3L_{L-1}) - E(^3L_{L+1})$  is very small, so that it is not necessary to know the energy difference to very high accuracy. As we will see below, our present measurements agree with theoretical predictions for the magnetic fine structure to within one part in ten thousand. In fact even an accuracy of one part per thousand leads to negligible errors in the calculation of the mean interval. We have therefore used the calculated values of the indicated triplet fine-structure interval [2] to compute the mean interval.

The agreement between the present and previous measurements is very good for the higher- $L$  intervals, but for the  $10G$ - $H$  interval there is a  $2.7\sigma$  discrepancy, which may be due to an underestimate of systematic corrections in the earlier measurement.

The most accurate calculations for these states are done by Drake using a variational technique [2,18,19]. A direct comparison between Drake's theory and measurements is also given in Table VII. The difference between experiment and theory is well outside of the error bars, and the theory is always larger than the experimental values. In the following paragraphs we will discuss in detail the comparison of our experimental values to the theory of Drake and to other theories. The comparison will be done in two parts, first comparing theory and experiment for the magnetic fine (or spin) structure (the structure within a particular  $L$ ) and then comparing the energy separations between states of different  $L$ , where the effects of retardation are expected.

To compare experiment and theory for the spin structure, we take the difference between the measured intervals and the mean intervals, as shown in Table VIII. This difference is entirely due to the relative spacing of the four spin-structure states within each  $L$ . There are several calculations of this spin structure. The variational calculations of Drake [19,2] include this structure, and his predictions for the structure show good agreement with experiment, as shown in column 3 of Table VIII. Calculations of Idrees [21], who uses a multiconfiguration Hartree-Fock method, show good agreement for the  $10H$ - $I$  intervals, but give poor agreement for the  $10G$ - $H$  intervals.

In addition to the above calculations, there are also some very different calculations, which derive the structure from the long-range interactions between the  $\text{He}^+$  ion and the distant Rydberg electron. These calculations have the advantage that their results can be written as very simple expressions, which can then be applied easily to any high- $L$  Rydberg state. The calculations of Cok and Lundeen [22], for the spin structure can be written in terms of the simple Hamiltonian [4]

$$H_{\text{spin}}^{BB} = \alpha^2 \left[ \frac{a_1}{2} \frac{\mathbf{L}_2 \cdot \mathbf{S}_2}{r_2^3} - a_2 \frac{\mathbf{L}_2 \cdot \mathbf{S}_1}{r_2^3} \right. \\ \left. + a_3 \frac{\mathbf{S}_1 \cdot \mathbf{S}_2 - 3(\mathbf{S}_1 \cdot \hat{\mathbf{r}}_2)(\mathbf{S}_2 \cdot \hat{\mathbf{r}}_2)}{r_2^3} \right], \quad (15)$$

where  $\alpha$  is the fine-structure constant,  $\mathbf{L}_2$  is the angular momentum of the outer electron,  $\mathbf{S}_1$  and  $\mathbf{S}_2$  are the spins of the core and Rydberg electrons,  $r_2$  and  $\hat{\mathbf{r}}_2$  are the distance and direction of the Rydberg electron relative to the nucleus, and the constants  $a_1$ ,  $a_2$ , and  $a_3$  are given by  $a_1 = (g-1) + 2gm/M \approx 1 + \alpha/\pi + 4m/M$ ,  $a_2 = g/2 \approx 1 + \alpha/2\pi$ , and  $a_3 = (g/2)^2 \approx 1 + \alpha/\pi$ , where  $m$  and  $M$  are the mass of the electron and the  $^4\text{He}$  nucleus.  $H_{\text{spin}}^{BB}$  is to be evaluated using the unsymmetrized wave functions

$$\Psi = \sum_{m_L, m_s} \psi_{1s}^{Z=2}(\mathbf{r}_1) \psi_{nLm_L}^{Z=1}(\mathbf{r}_2) |S, m_s\rangle \\ \times \langle L, m_L, S, m_s | L, S, J, m_J \rangle.$$

The corrections which result from the fact that the wave functions are not perfectly hydrogenic have been calculated by Cok [22], and are negligible for  $L \geq 5$ .

In addition to the  $H_{\text{spin}}^{BB}$  contributions, there are also small contributions due to exchange which alter the spacing of the four states at lower  $L$ . The exchange energy contributes  $(-1)^S V_x$ , where  $V_x$  is given to first order by

$$V_x = \langle \psi_{1s}^{Z=2}(\mathbf{r}_1) \psi_{nLm_L}^{Z=1}(\mathbf{r}_2) | 1/r_{12} \\ - 1/r_2 | \psi_{1s}^{Z=2}(\mathbf{r}_2) \psi_{nLm_L}^{Z=1}(\mathbf{r}_1) \rangle.$$

From this equation one obtains  $V_x(10G) = 100$  kHz,  $V_x(10H) = 0.21$  kHz, and  $V_x(10I) = 0.0004$  kHz. How-

TABLE VIII. A comparison between experiment and theory for the magnetic fine structure (MFS) of helium  $n = 10$  states. The table gives the difference between the measured intervals and the mean intervals for each of the 16 measured intervals, as well as the  $10F$ - $G$  measurements of Ref. [6]. The calculations of Drake [19,2], Idrees [21], Pilkuhn [20], and Cok [22] for these contributions are listed, and compared to theory. The values of reduced  $\chi^2$  listed indicate the level of agreement between experiment and the various predictions. All values are in MHz and one standard deviation errors are given in parentheses.

Interval	Frequency of particular MFS component relative to the separation between the mean energies (MHz)				
	Measured	Drake [2]	Idrees [21]	Pilkuhn [20]	Cok [22,4]
$+F_3^-+G_4$	-19.248 0(38)	-19.249 0			
${}^3F_2^-{}^3G_3$	+1.337 1(52)	+1.336 6			
${}^3F_4^-{}^3G_5$	+8.411 3(45)	+8.414 4			
$-F_3^-G_4$	+6.879 1(56)	+6.876 8			
$\chi_{\text{reduced}}^2$		0.2			
$+G_4^-+H_5$	-4.146 56(64)	-4.146 95	-4.1488	-4.1457	-4.1441
${}^3G_3^-{}^3H_4$	-2.341 04(82)	-2.341 91	-2.3394	-2.3434	-2.3378
${}^3G_5^-{}^3H_6$	+0.958 11(56)	+0.957 99	+0.9604	+0.9590	+0.9554
$-G_4^-H_5$	+4.548 37(66)	+4.549 62	+4.5464	+4.5483	+4.5468
$\chi_{\text{reduced}}^2$		1.3	10.4	3.3	14.4
$+H_5^-+I_6$	-2.384 57(33)	-2.385 09	-2.3850	-2.3848	-2.3848
${}^3H_4^-{}^3I_5$	-1.238 02(39)	-1.238 65	-1.2383	-1.2389	-1.2383
${}^3H_6^-{}^3I_7$	+0.576 39(29)	+0.576 88	+0.5767	+0.5769	+0.5766
$-H_5^-I_6$	+2.595 45(35)	+2.595 90	+2.5959	+2.5957	+2.5957
$\chi_{\text{reduced}}^2$		2.4	2.1	1.1	0.4
$+I_6^-+K_7$	-1.503 34(37)	-1.502 73		-1.5027	-1.5026
${}^3I_5^-{}^3K_6$	-0.728 81(41)	-0.729 24		-0.7293	-0.7290
${}^3I_7^-{}^3K_8$	+0.380 13(27)	+0.379 93		+0.3800	+0.3797
$-I_6^-K_7$	+1.615 53(33)	+1.615 50		+1.6154	+1.6155
$\chi_{\text{reduced}}^2$		1.1		1.3	1.5
$+K_7^-+L_8$	-1.007 16(46)			-1.0077	-1.0077
${}^3K_6^-{}^3L_7$	-0.466 45(62)			-0.4652	-0.4650
${}^3K_8^-{}^3L_9$	+0.263 54(43)			+0.2534	+0.2632
$-K_7^-L_8$	+1.073 82(45)			+1.0734	+1.0733
$\chi_{\text{reduced}}^2$				1.6	3.8

ever, it is known that these first-order estimates are not reliable, and Poe and Chang have calculated  $V_x(G)=32$  kHz and  $V_x(H)=0$  kHz [23]. Very reliable exchange energies can be had from the calculations of Drake [2], who gets  $V_x(G)=41.726$  kHz,  $V_x(H)=0.076$  kHz, and  $V_x(I)=0.0001$  kHz. The predictions of Cok (including these exchange energies) are listed in Table VIII.

Pilkuhn [20] calculates the magnetic fine structure from a long-range-interaction point of view, in which he treats the  $\text{He}^+$  core as a single particle with mass  $M+m$ , charge  $+e$ , and magnetic moment  $-g\mu_B/2$ . His predictions for the structure are listed in column 5 of Table VIII, and show acceptable agreement for the higher- $L$  intervals. The results of Pilkuhn [20] can also be put in the form of the operator  $H_{\text{spin}}^{BB}$  of Eq. (15). The constants  $a_1$ ,  $a_2$ , and  $a_3$  which result from his calculations are  $a_1=1+\alpha/\pi+2m/M$ ,  $a_2=1+\alpha/2\pi+m/M$ , and  $a_3=1+\alpha/\pi$ . These differ from the values given in Cok's model by terms of order  $m/M$ . This discrepancy is not surprising since the Cok model does not include the effects of the mass-polarization operator on the magnetic fine structure. A comparison between the Pilkuhn and

Drake MFS predictions at high  $L$ , where both are expected to be quite accurate, gives a strong test of the two very different theories. They are found to agree to the 10 Hz level for the  $10K$  state, which instills confidence in the results of both theories and, in particular, indicates that Pilkuhn seems to have the proper mass corrections, and can be used to predict the structure for states which Drake has not calculated. The predictions of Pilkuhn (including  $V_x$  for lower- $L$  states) are given in Table VIII. The agreement between Pilkuhn's predictions and experiment is good.

The precision of the measurements of the magnetic fine structure (of about  $10^{-4}$ , see Table VIII) is sufficient to see the  $\alpha^3\mathcal{R}$  anomalous moment corrections ( $\mathcal{R}$  is the Rydberg constant), and is approaching the level of accuracy needed for seeing the  $\alpha^4\mathcal{R}$  effects on the magnetic structure. The present measurements do not give very accurate information on the  $\alpha^4\mathcal{R}$  contributions; however, future measurements of slightly higher accuracy should be able to measure these effects.

We now turn to the energy intervals between states of different  $L$ , which has been the primary objective of these

measurements. Since states of different  $L$  sample different regions of the radial coordinate, these energy differences reflect many aspects of the interaction between the Rydberg electron and the  $\text{He}^+$  ion. One such interaction is the "retardation" interaction first discussed by Kelsey and Spruch [11] and later refined by Au, Feinberg, and Sucher [13] and by Babb and Spruch [24]. In order to resolve this subtle effect, which produces only small changes in the fine-structure intervals, it is necessary to understand all other contributions quite precisely.

A central theme in the theoretical progress towards this goal is the interplay between two quite different viewpoints on the helium Rydberg state. One view, which we call the long-range-interactions (LRI) view, treats the system as an electron interacting at a distance with a  $\text{He}^+$  ion. The other, more conventional view, treats the system as just another two-electron atom using standard atomic theory to describe the structure. Great progress has been achieved with both views over the past decade, and frequently the interplay between the two contrasting viewpoints has been an important factor in this progress.

Taking first the LRI point of view, the results of these calculations can be expressed as simple effective potentials and thus the energies of any high- $L$  Rydberg state can easily be calculated once these potentials are known. The dominant terms [25] from this point of view are

$$\left\langle \frac{(1/2)\alpha_1}{r^4} - \frac{1/2(\alpha_2 - 6\beta_1)}{r^6} \right\rangle, \quad (16)$$

where  $\alpha_1 = 9/32$ ,  $\alpha_2 = 15/64$ , and  $\beta_1 = 43/512$  are the dipole polarizability, quadrupole, polarizability, and nonadiabatic dipole polarizability, respectively. The full nonrelativistic energy predictions of Drachman [1] (including reduced-mass corrections [26]) are given in Table IX.

In the long-range model, the relativistic corrections are due to the standard  $p^4$  term:

$$\frac{\alpha^2}{2n^3} \left[ \frac{3}{4n} - \frac{1}{L + 1/2} \right], \quad (17)$$

with appropriate reduced-mass corrections [27,28], as well as relativistic corrections to the polarizabilities [29]. The leading term for the latter is

$$2\alpha^2 \frac{28}{27} \frac{\alpha_1}{r^4}. \quad (18)$$

The relativistic corrections to  $\beta_1$  have not yet been calculated. The dipole polarizability is also affected by the core electron Lamb shift. Since the  $\text{He}^+$  core is polarized, it is not in a pure  $1S$  state, but has some  $P$  character. This effect leads to a potential of

TABLE IX. Calculated contributions to the intervals between the mean  $n = 10$  states. All values are in MHz, with one standard deviation errors in parentheses.

Term	Contribution to the interval $L_{\text{mean}} - (L+1)_{\text{mean}}$ (MHz)				
	10F-G	10G-H	10H-I	10I-K	10K-L
Long-range-interaction picture					
$E_{nr}$	2100(100)	484.0(5)	152.19(1)	57.2392(4)	24.4347(2)
$p^4$	11.1220	7.0774	4.8997	3.5931	2.7477
$\Delta\alpha_{\text{rel}}$	-0.4578	-0.1080	-0.0338	-0.0127	-0.0054
$\langle V_{\text{ret}} \rangle$	-0.1853	-0.0422	-0.0126	-0.0045	-0.0018
$\Delta_{\text{core LS}}$	0.0584	0.0138	0.0043	0.0016	0.0007
Total <sup>a</sup>	2036.5178 <sup>a</sup>	491.0014 <sup>a</sup>	157.0522 <sup>a</sup>	60.8163 <sup>a</sup>	27.1759(2)
Expt.	2036.5590(22)	491.0052(5)	157.0524(2)	60.8160(2)	27.1747(5)
Expt. minus theor.	-0.0412(22)	0.0038(5)	0.0002(2)	-0.0003(2)	-0.0012(5)
Standard atomic theory picture (Drake)					
$E_{nr}$	2025.9805	484.06044	152.19464	57.23879	
$\Delta E_{\text{rel}}$	10.5268(3)	6.93006(10)	4.85278(5)	3.57532(1)	
$L1$	0.0546	0.01286	0.00396	0.00145	
$L2$	0.0123	0.00484	0.00228	0.00122	
$\langle V''_{\text{ret}} \rangle$	-0.0012	-0.00071	-0.00045	-0.00030	
Total	2036.5730(3)	491.00750(10)	157.05321(5)	60.81647(1)	
Expt.	2036.5590(22)	491.00523(49)	157.05241(23)	60.81595(20)	
Expt. minus theor.	-0.0140(22)	-0.00227(50)	-0.00080(24)	-0.00052(20)	

<sup>a</sup>Since the nonrelativistic energies are poorly determined for the lower- $L$  interval the precise nonrelativistic energies of Drake are used to calculate the total energies for these intervals.

$$-\frac{31}{36}\mathcal{L}(\text{He}^+ 1S)\frac{\alpha_1}{r^4}, \quad (19)$$

where  $\mathcal{L}(\text{He}^+ 1S)$  is the Lamb shift (in atomic units) for the  $1S$  state of  $\text{He}^+$ . The contributions to the  $n=10$  intervals are given in Table IX. Finally, since none of the long-range potentials mentioned have contributions due to retardation, the full retardation potential  $V_{\text{ret}}$  must be used. These contributions [30,24] are also listed in Table IX.

In order to make a high-precision comparison between experiment and theory, the very accurate nonrelativistic energies of Drake are used in place of the less accurate polarization-potential energies of Drachman for the lower- $L$  intervals. (This substitution is possible since the nonrelativistic Coulomb Hamiltonian is treated separately from relativistic and radiative effects in both calculations.) The comparison between experiment and theory at higher- $L$  reveals surprisingly good agreement. A significant consequence of this good agreement is that the effects of retardation are verified to the level of about ten percent or better for the  $10G-H$ ,  $10H-I$ , and  $10I-K$  intervals. The remaining discrepancies probably indicate that other relativistic corrections remain to be accounted for in this approach.

Table IX also shows the rather different breakdown of the energy contributions which one obtains from the standard atomic theory calculations of Drake. The calculations of Drake include the nonrelativistic energy  $E_{\text{nr}}$ , which he calculates very accurately, the relativistic corrections  $\Delta E_{\text{rel}}$ , which come from the  $\alpha^2$  relativistic corrections arising from the nonrelativistic reductions of the Breit and Dirac operators, and  $L1$  and  $L2$ , the one- and two-electron Lamb shifts. To the total theory of Drake, we must add those effects of retardation which Drake has not included. In 1984, Au, Feinberg, and Sucher [13] showed that this asymptotic potential of Kelsey and Spruch [11] is not appropriate for  $n=10$  states, and calculated the retardation potential at shorter distances. It was subsequently shown [24] that the retardation potential could be expanded in terms of increasing powers of  $Z^2 ar/a_0 \approx r/35a_0$  as

$$V_{\text{ret}}^{\text{AFS}} = \frac{\alpha^2 a_0^4}{Z^2 r^4} \left[ 1 - \frac{7}{6\pi} (Z^2 ar/a_0) + \frac{1}{3} (Z^2 ar/a_0)^2 + \dots \right] \frac{e^2}{a_0}. \quad (20)$$

The convergence of this series might be expected to be very poor since the majority of the wave function is in the region  $r > 35a_0$ . However, since  $V_{\text{ret}}$  decreases very rapidly with  $r$ , the largest part of  $|\Psi|^2 V_{\text{ret}}$  is in the region  $r < 35a_0$ , and as a result, the convergence, while not great, is not as poor as one may have expected. It has been shown [31] that the first term of this expansion (the  $r^{-4}$  term) comes from a second-order correction involving  $H_2$  (the retardation term in the Breit interaction [32]) and a Coulomb photon, and as such is included in the calculations of Drake. The second ( $r^{-3}$ ) term has been identified with the so-called  $Q$  term, a QED term which

makes up most of what Drake refers to as the two-electron Lamb shift. The remainder of the retardation potential is referred to as  $V_{\text{ret}}''$  and is given by

$$V_{\text{ret}}'' = V_{\text{ret}}^{\text{AFS}} - \frac{\alpha^2 a_0^4}{Z^2 r^4} \left[ 1 - \frac{7}{6\pi} (Z^2 ar/a_0) \right] \frac{e^2}{a_0}. \quad (21)$$

As discussed by Au and Mesa [31,30] and Drake [19], this potential is not included in the Drake's calculations and thus Drake's results should be corrected by the expectation value of this potential. Although the experimental errors are slightly smaller than the  $V_{\text{ret}}''$  corrections, the agreement between experiment and theory is too poor to test the  $V_{\text{ret}}''$  effects.

The comparison between experiment and the theory of Drake show significant discrepancies as shown in the final row of Table IX. These discrepancies are larger than the  $V_{\text{ret}}''$  effects and are not presently understood. Whether these discrepancies are due to errors in the calculations of  $V_{\text{ret}}$  or of the radiative or relativistic corrections for these states, or whether they are due to some other effect in these large atoms is unknown.

It is intriguing to note that the difference between experiment and the best theory (the long-range-interaction predictions for the  $K-L$  interval and Drake  $+V_{\text{ret}}''$  for the lower- $L$  intervals) is always negative. The fractional residuals ( $E-T/T$ ) are  $-6.9 \pm 1.1$ ,  $-4.6 \pm 1.0$ ,  $-5.1 \pm 1.5$ ,  $-8.5 \pm 3.3$ , and  $-44 \pm 20$  ppm for the  $10F-G$ ,  $G-H$ ,  $H-I$ ,  $I-K$ , and  $K-L$  intervals, respectively. These are all reasonably consistent with a  $-5.3 \pm 0.6$  ppm residual, suggesting that there is some contribution which has been left out of the calculations. From the pattern of the residuals, we can try to determine what the form of this missing contribution might be. If we assume that the contribution is proportional to  $r^n$ , the only  $n$  which can match the pattern of the residuals is  $n=-4$ , and the missing term is thus consistent with a small term of this form equivalent to a  $-5.3 \pm 0.6$  ppm correction in the dipole polarizability of the  $\text{He}^+$  core. Perhaps this correction is due to QED contributions [other than the Lamb-shift correction of Eq. (19)] to the dipole polarizability.

Another quite different explanation of the residuals could be due to a correction to the Coulombic  $1/r$  potential on the distance scales of these Rydberg states. Bartlett has investigated [33] the limits on such a "fifth force of electrostatics" for potentials of the form

$$\frac{e^2}{r} (1 + \beta e^{-r/\lambda}). \quad (22)$$

One can easily calculate the effect of such a modified potential for the  $n=10$  Rydberg states using perturbation theory, and one finds that the pattern of the perturbations (as a function of  $L$ ) does not match our pattern of the observed residuals for any choice of  $\beta$  and  $\lambda$ . It is interesting to note, however, that our data provide slightly better limits on this fifth force for distance scales of  $(50-2000)a_0$  than those given by Bartlett [34].

In summary, the very accurate measurements of these high- $L$   $n=10$  intervals in helium have been used to study many aspects of these large-sized, simple two-electron atoms. The measurements give good agreement (at the

100 ppm level) with the predicted spin structure for these states. The experimental values for the separation of states of different  $L$  agree to within about ten parts per million with both the predictions of the standard atomic theory of Drake and the long-range-interaction calculations of Drachman. However, in both cases, there are statistically significant differences between experiment and theory, indicating the presence of physical effects not included in the present calculations. These differences with the most precise calculations could be explained by

a  $-5.3 \pm 0.6$  ppm change in the dipole polarizability of  $\text{He}^+$ , perhaps due to QED effects. These measurements test the retardation contributions to these states to better than 10% and provide an observation of microscopic retardation effects at this precision.

#### ACKNOWLEDGMENT

This work was supported by the National Science Foundation under Grant No. PHY90-19064.

\*Present address: Department of Physics and Astronomy, York University, 4700 Keele Street, North York, Ontario, Canada M3J 1P3.

†Present address: Department of Physics, Occidental College, Los Angeles, CA 90041.

- [1] Richard J. Drachman, *Phys. Rev. A* **31**, 1253 (1985).
- [2] G. W. F. Drake, *Phys. Rev. Lett.* **65**, 2769 (1990).
- [3] S. L. Palfrey and S. R. Lundeen, *Phys. Rev. Lett.* **53**, 1141 (1984).
- [4] E. A. Hessels, W. G. Sturuss, S. R. Lundeen, and David R. Cok, *Phys. Rev. A* **35**, 4489 (1987).
- [5] E. A. Hessels, W. G. Sturuss, and S. R. Lundeen, *Phys. Rev. A* **38**, 4574 (1988).
- [6] E. A. Hessels, F. J. Deck, P. W. Arcuni, and S. R. Lundeen, *Phys. Rev. A* **41**, 3663 (1990); **44**, 7855 (1991).
- [7] E. A. Hessels, F. J. Deck, P. W. Arcuni, and S. R. Lundeen, *Phys. Rev. Lett.* **65**, 2765 (1990); **66**, 2544 (1991).
- [8] H. B. G. Casimir and D. Polder, *Phys. Rev.* **73**, 360 (1948).
- [9] James F. Babb and Larry Spruch, *Phys. Rev. A* **36**, 456 (1987).
- [10] Larry Spruch, *Phys. Today* **39** (11), 37 (1986).
- [11] Edward J. Kelsey and Larry Spruch, *Phys. Rev. A* **18**, 15 (1978).
- [12] R. J. Drachman, *Phys. Rev. A* **26**, 1228 (1982).
- [13] C. K. Au, G. Feinberg, and J. Sucher, *Phys. Rev. Lett.* **53**, 1145 (1984).
- [14] S. L. Palfrey, Ph.D. thesis, Harvard University, 1983 (unpublished).
- [15] H. A. Bethe and E. E. Salpeter, *Quantum Mechanics of One- and Two-Electron Atoms* (Plenum, New York, 1977), p. 207.
- [16] J. W. Farley and W. H. Wing, *Phys. Rev. A* **23**, 2397 (1981).
- [17] J. W. Farley, K. B. MacAdam, and W. H. Wing, *Phys. Rev. A* **20**, 1754 (1979); **25**, 1790 (1982).
- [18] G. W. F. Drake, *Phys. Rev. Lett.* **59**, 1549 (1987).
- [19] G. W. F. Drake, *J. Phys. B* **22**, L651 (1989); **23**, 1943 (1990).
- [20] M. Martinis and H. Pilkuhn, *J. Phys. B* **15**, 1797 (1982).
- [21] M. Idrees and C. F. Fischer, *Nucl. Instrum. Methods B* **42**, 552 (1989).
- [22] D. R. Cok and S. R. Lundeen, *Phys. Rev. A* **19**, 1830 (1979); **24**, 3283 (1981).
- [23] T. N. Chang and R. T. Poe, *Phys. Rev. A* **10**, 1981 (1974); T. N. Chang (private communication).
- [24] James F. Baab and Larry Spruch, *Phys. Rev. A* **38**, 13 (1988).
- [25] Richard J. Drachman, *Phys. Rev. A* **26**, 1228 (1982).
- [26] Richard J. Drachman, *Phys. Rev. A* **33**, 2780 (1986).
- [27] Richard J. Drachman, *Phys. Rev. A* **42**, 5762(E) (1990).
- [28] C. K. Au, G. Feinberg, and J. Sucher, *Phys. Rev. A* **43**, 561 (1991).
- [29] Richard J. Drachman, *Phys. Rev. A* **37**, 979 (1988).
- [30] C. K. Au and M. A. Mesa, *Phys. Rev. A* **41**, 2848 (1990).
- [31] C. K. Au and M. A. Mesa, *Phys. Rev. A* **39**, 2789 (1989).
- [32] H. A. Bethe and E. E. Salpeter, *Quantum Mechanics of One- and Two-Electron Atoms* (Ref. [15]), p. 182.
- [33] D. F. Bartlett and Stefan Logl, *Phys. Rev. Lett.* **61**, 2285 (1988).
- [34] The  $10I$ - $K$  measurement puts limits of  $6 \times 10^{-10}$ ,  $3 \times 10^{-9}$ , and  $2 \times 10^{-8}$  on the parameter  $\beta$  in the non-Coulombic potential  $e^2/r(1 + \beta e^{-r/\lambda})$ , for distance scale of  $\lambda = 100, 300$ , and  $1000a_0$ . These are slightly smaller than the limits of  $1 \times 10^{-9}$ ,  $6 \times 10^{-9}$ , and  $7 \times 10^{-8}$  derived by Bartlett from precision measurements of the Rydberg constant.